



TECHNICAL UNIVERSITY OF LIBEREC
Faculty of Mechatronics, Informatics
and Interdisciplinary Studies ■

Advanced Calibration and Characterization of a Shack-Hartmann Sensor

Master thesis

M18000173

Study programme: N 3901 – Applied Sciences in Engineering
Study branch: 3901T055 – Applied Sciences in Engineering
Author: **Bc. Martin Dušek**
Supervisor: Ing. Vít Lédl Ph.D





Zadání diplomové práce

Advanced Calibration and Characterization of a Shack-Hartmann Sensor

Jméno a příjmení: **Bc. Martin Dušek**
Osobní číslo: M18000173
Studijní program: N3901 Aplikované vědy v inženýrství
Studijní obor: Aplikované vědy v inženýrství
Zadávací katedra: Ústav nových technologií a aplikované informatiky
Akademický rok: **2019/2020**

Zásady pro vypracování:

1. Elaborate a theoretical recherche focused on the principle of the Shack-Hartmann sensor for a wavefront characterization.
2. Develop a software for reconstruction of the wavefront using the Shack-Hartmann sensor based on the recherche, focus on the possibilities of calibration and characterization of the sensor.
3. Elaborate an analysis of potential problems and principal limitations of the sensor and the software.
4. Perform test measurements, evaluate results and compare the algorithms for the wavefront reconstruction.

Rozsah grafických prací:
Rozsah pracovní zprávy:
Forma zpracování práce:
Jazyk práce:

dle potřeby dokumentace
40 – 50 stran
tištěná/elektronická
Angličtina



Seznam odborné literatury:

- [1] M.Born, E.Wolf. *Principles of optics*, 6th ed. Pergamon Press, New York, 1980.
- [2] Geary, Joseph M, *Introduction to wavefront sensors*, SPIE Optical Engineering Press Bellingham, Wash., USA, 1995.
- [3] J. Novak, P. Novak, A. Misk. „Application of Shack-Hartmann wavefront sensor for testing optical systems,“ *Proceedings of SPIE – The International Society for Optical Engineering*, 6609, 2007.

Vedoucí práce:

Ing. Vít Lédl, Ph.D.
TOPTEC, Ústav fyziky plazmatu AV ČR, v. v. i., výkonný ředitel

Datum zadání práce:

9. října 2019

Předpokládaný termín odevzdání:

17. května 2021

prof. Ing. Zdeněk Plíva, Ph.D.
děkan

L.S.

Ing. Josef Novák, Ph.D.
vedoucí ústavu

Prohlášení

Prohlašuji, že svou diplomovou práci jsem vypracoval samostatně jako původní dílo s použitím uvedené literatury a na základě konzultací s vedoucím mé diplomové práce a konzultantem.

Jsem si vědom toho, že na mou diplomovou práci se plně vztahuje zákon č. 121/2000 Sb., o právu autorském, zejména § 60 – školní dílo.

Beru na vědomí, že Technická univerzita v Liberci nezasahuje do mých autorských práv užitím mé diplomové práce pro vnitřní potřebu Technické univerzity v Liberci.

Užiji-li diplomovou práci nebo poskytnu-li licenci k jejímu využití, jsem si vědom povinnosti informovat o této skutečnosti Technickou univerzitu v Liberci; v tomto případě má Technická univerzita v Liberci právo ode mne požadovat úhradu nákladů, které vynaložila na vytvoření díla, až do jejich skutečné výše.

Současně čestně prohlašuji, že text elektronické podoby práce vložený do IS/STAG se shoduje s textem tištěné podoby práce.

Beru na vědomí, že má diplomová práce bude zveřejněna Technickou univerzitou v Liberci v souladu s § 47b zákona č. 111/1998 Sb., o vysokých školách a o změně a doplnění dalších zákonů (zákon o vysokých školách), ve znění pozdějších předpisů.

Jsem si vědom následků, které podle zákona o vysokých školách mohou vyplývat z porušení tohoto prohlášení.

27. května 2021

Bc. Martin Dušek

Acknowledgements

I would like to express my special thanks of gratitude to my supervisor Ing. Vít Lédl Ph.D. for guiding my direction and for the opportunity to work on the topic. I'm also really thankful to Ing. Marek Stašík for his valuable advice and consultations and to Ing. Pavel Psota Ph.D. for the feedback he gave me.

I would also like to extend my appreciation to the whole Research Centre for Special Optics and Optoelectronic Systems TOPTEC for providing me all the necessary tools and equipment while working on the thesis.

Secondly I would also like to thank my family and people that are close to me for the support they provided me during the studies.

Advanced Calibration and Characterization of a Shack-Hartmann Sensor

Abstract

The main goal of the Master's thesis is the development of the software and also of the calibration routine for the Shack-Hartmann sensor. The principle of the reconstruction was closely analyzed including the principal limitations. The most effective reconstruction procedures were chosen from the already existing methods. These are described in the theoretical part in great detail.

Two reconstruction algorithms and four algorithms for the detection of the centroids of the intensity spots were implemented, based on the theoretical basis. Furthermore the novel calibration routine was also developed including the accompanying algorithm. It provides compensation for the construction errors of the sensor, which leads to the high precision of the reconstruction of a wavefront.

The precision and time effectiveness of the algorithms were analyzed by experiments and simulations. Results of the reconstructions were compared to results of the commercial software. It can be said, that the developed software is equally precise and in some cases even surpasses the commercial software.

The software was used for the analysis of the results from the experimental method for an automatic alignment of the multi-lens optical system. The accuracy of the outcome was confirmed by comparing the results with the simulations carried out with Zemax. In addition the experiment showed, that the software can be used for real-time reconstruction. It was possible to reconstruct the wavefront of the Structured beam for the first time. The beam has been patented in the collaboration of the leading scientific organizations TOPTEC and CERN in the last few years. The commercial software failed in this task.

Keywords: Shack-Hartmann sensor, calibration, MATLAB, wavefront

Pokročilá kalibrace a charakterizace Shack-Hartmannova senzoru

Abstrakt

Hlavním cílem práce je vývoj softwaru a kalibračního postupu pro Shack-Hartmannův senzor. Princip rekonstrukce byl důkladně zanalyzován včetně principiálních omezení. Z již existujících postupů rekonstrukce vlnoplochy byly vybrány ty nejefektivnější. Ty jsou v teoretické části práce detailně popsány.

Na základě teoretické rešerše byly implementovány rekonstrukční algoritmy a čtyři algoritmy pro detekci center intenzitních stop. Dále byl vyvinut optimalizovaný postup kalibrace včetně doprovodného algoritmu. Ten zajišťuje kompenzaci konstrukčních chyb senzoru, což vede k vysoké přesnosti rekonstrukce vlnoplochy.

Přesnost a časová náročnost algoritmů byla analyzována pomocí experimentů a simulací. Výsledky rekonstrukcí byly porovnány s komerčním softwarem. Lze konstatovat, že vyvinutý software dosahuje srovnatelné přesnosti rekonstrukce a v některých případech komerční software i předčí.

Software byl použit pro analýzu výsledků experimentální metody pro automatickou justaci komplexního optického systému s více čočkami. Zde se potvrdila jeho přesnost při porovnání výsledků se simulacemi z programu Zemax. Experiment také ukázal, že je možné použít software pro rekonstrukci v reálném čase. Dále se podařilo poprvé zrekonstruovat vlnoplochu Strukturovaného svazku, který byl v posledních letech patentován ve spolupráci špičkových vědeckých pracovišť TOPTEC a CERN. Komerční software v tomto úkolu selhal.

Klíčová slova: Shack-Hartmannův senzor, kalibrace, MATLAB, vlnoplocha

Contents

List of Abbreviations	10
List of Figures	12
List of Tables	13
List of Symbols	15
Introduction	16
1 Rays and Wavefronts	17
1.1 Optical systems	19
1.2 Zernike polynomials	19
2 Background for Wavefront Sensing	21
2.1 Operating principle of the Shack-Hartmann wavefront sensor	22
2.2 Detection of the spot centroids	24
2.3 Wavefront reconstruction methods	25
2.3.1 Modal wavefront reconstruction	25
2.3.2 Zonal wavefront reconstruction	26
2.4 Principal limitations of the sensor	28
3 Implementation of the Wavefront Reconstruction in MATLAB	29
3.1 Algorithms for the detection of the spot centroids	30
3.1.1 Thresholding	31
3.1.2 Gamma correction	31
3.1.3 Windowing	32
3.1.4 Correlation	33
3.2 Calibration of the reference centroids	33
3.3 Calibration of the normalization factors	35
3.4 Algorithms for the wavefront fitting	40
3.4.1 Modal fitting routine	40
3.4.2 Zonal fitting routine	41
4 Analysis of the Algorithms	42
4.1 Simulation environment	42
4.1.1 Comparison of the algorithms for the detection of spot centroids via simulation	42
4.1.2 Comparison of the algorithms for wavefront fitting via simulation	44
4.2 Comparison of the presented reconstruction software with the commercial software	45
4.2.1 Reconstruction of the plane wavefront	46
4.2.2 Reconstruction of the spherical wavefront	47

	4.2.3	Reconstruction of the wavefront A	48
	4.2.4	Reconstruction of the wavefront B	50
5		Application of the Algorithm for Alignment of the Complex Optical System	51
	5.1	Description of the adjusted complex optical system	52
	5.2	.NET library for C# application	53
	5.3	Alignment of the complex optical system	54
6		Application of the Algorithm for Wavefront Reconstruction of the Structured Beam	56
	6.1	Wavefront reconstruction of the Structured beam	57
7		Conclusions	60
		Bibliography	62

List of Abbreviations

CoG	Center of Gravity
OPL	Optical path length
OPD	Optical path difference
OTF	Optical transfer function
RMSe	Root mean square error
RoC	Radius of curvature
ROI	Region of interest
SHWS	Shack Hartmann wavefront sensor
SNR	Signal-to-noise ratio

List of Figures

2.1	Illustration of perfect spherical and plane waves	17
2.2	Reflection and refraction of the ray incident on to the interface of materials with different refractive indices	18
2.3	The ideal optical system	19
2.4	Illustration of the aberrated wavefront on the output of a real optical system.	19
2.5	Surface plots of first 6 Zernike polynomials	21
3.6	Hartmann mirror test and illustration of relation between rays and wavefront aberrations	22
3.7	Working principle of a Shack-Hartmann sensor	23
3.8	The shift of the spot from the reference position, which is caused by the change of the wavefront slope.	23
3.9	Intensity distribution of the diffracted spot imaged on to the CCD sensor.	24
3.10	Southwell geometry for wavefront estimation scheme	27
3.11	Illustration of the multiple spots in one ROI.	28
3.12	Illustration of the smoothing effect of a wavefront with high spatial frequency.	29
4.13	Basic structure of the software.	30
4.14	Examples of spotimages generated with the simulation environment	31
4.15	Output of gamma correction	32
4.16	Example of windowing used in a noisy ROI.	32
4.17	Illustration of correlation centroiding	33
4.18	Logic of the reference spot position algorithm calibration.	34
4.19	Illustration of the reference calibration process.	35
4.20	The illustration of the normalization factor dependence on the aperture size	36
4.21	Spots created by perfectly spherical wavefront.	37
4.22	Photo of the calibration process	38
4.23	Set of measurements of the spherical wavefronts with different radii and the fit of the second-order polynomial.	39
4.24	Logic of the algorithm for normalization factor calibration.	40
4.25	Logic of the modal and zonal fitting algorithms	41
4.26	Zonal wavefront reconstructions	42
5.27	Comparison of the algorithms for the detection of spot centroids without and with windowing	43

5.28	Example of a reference and reconstructed coefficients used in simulations.	45
5.29	Results of the almost perfectly plane wavefront reconstruction.	47
5.30	Reconstructed Zernike coefficients of the almost perfectly spherical wavefront.	48
5.31	Reconstruction of the wavefront A generated by a experimental optical system.	49
5.32	Reconstruction of the wavefront B generated by the experimental optical system with induced defocus.	51
6.33	Perfectly aligned optical system.	52
6.34	Examples of misaligned optical systems	52
6.35	The model of the experimental multi-lens optical system generated in Zemax software	53
6.36	Photo of the multi-lens complex optical system	54
6.37	The wavefront on the output of the modeled optical system, generated by Zemax.	55
6.38	The wavefront on the output of the real optical system measured in the laboratory.	55
7.39	Generation of a Bessel beam using a axicon	56
7.40	Illustration of a self regenerating ability of Bessel beams	56
7.41	Simulation of a wavefront of a Structured beam using VirtualLab Fusion	57
7.42	Reconstructed wavefront of the Structured beam using the Thorlabs software	58
7.43	Spotimage generated by a Structured beam	58
7.44	Wavefront of the Structured beam reconstructed using the presented software.	59

List of Tables

5.3	Time efficiency of the centroiding algorithms after analyzing 1640 ROIs.	43
5.4	The $RMSe$ computed from the difference between the input coefficients and the fitted ones.	44
5.5	Time efficiency of the fitting algorithms.	45
5.6	Specifications of the wavefront sensor used and hardware limitations of the wavefront reconstruction	46
5.7	The $RMSe$, hence the noise of the algorithms used to reconstruct almost perfectly plane wavefront.	47
5.8	The $RMSe$, hence the noise of the algorithms used to reconstruct almost perfectly spherical wavefront.	48
5.9	The $RMSe_{diff}$ of the algorithms calculated from the difference of the fitted coefficients when reconstructing wavefront A.	49
5.10	The $RMSe_{diff}$ of the algorithms calculated from the difference of the fitted coefficients when reconstructing wavefront B.	51

List of Symbols

c	[m/s]	Speed of light in a vacuum
\mathbf{c}		Column vector of Zernike coefficients
C		Sparse rectangular matrix used for zonal reconstruction
C_j	[m]	Single indexed coefficients of Zernike polynomials
C_n^m	[m]	Double indexed coefficients of Zernike polynomials
col		Index of a column on a CCD sensor
d	[m]	Microlens diameter
D		Matrix of partial derivatives of Zernike polynomials
D_{airy}	[m]	Diameter of a Airy disk
D_{aper}	[m]	Aperture diameter
E		Sparse rectangular matrix used for zonal reconstruction
f	[m]	Focal length
$I(row, col)$		Function of intensity
\mathbf{k}	[rad/m]	Wave vector
k_0	[rad/m]	Wave number
n		Refractive index
N_{modal}		Normalization factor of modal reconstruction
N_{zonal}		Normalization factor of zonal reconstruction
N_{std}		Standart deviation of the intensity value of all pixels in the pictures
N_n^m		Double indexed normalization factor of Zernike polynomials
P	[m]	Lens pitch
Q	[m]	Distance between centroids when with a spherical wavefront incident
\mathbf{r}	[m]	Position vector
R	[m]	Radius of curvature
R_n^μ		Radial polynomials
row		Index of a row on a CCD sensor
RMS_e	[m]	Root mean square error
$RMS_{e,diff}$	[m]	Root mean square error difference
s		Matrix of slopes
\mathbf{s}		Unit vector
s_{pix}	[m]	Pixel size
$S(\mathbf{r})$	[m]	Eikonal
S_{mean}		Mean intensity value of all pixels in the picture
$S_{row,col}^X$		Slope of a wavefront in x direction
$S_{row,col}^Y$		Slope of a wavefront in y direction

SNR		Signal-to-noise ratio
SNR_{dB}	[dB]	Signal-to-noise ratio expressed in decibels
$T(row, col)$		Thresholding function
TA_x	[m]	Transverse shift of a spot in x direction
TA_y	[m]	Transverse shift of a spot in y direction
$U(\mathbf{r}, t)$		Complex wave function
$U_n^m(r, \theta)$		Double indexed Zernike polynomials
v	[m/s]	Speed of light in a medium
\mathbf{w}		Column vector of wavefront phase values
$W(r, \theta)$		Function representing OPD of a wavefront
\bar{x}		Centroid coordinate of a spot in x direction
\bar{y}		Centroid coordinate of a spot in y direction
$Z_j(r, \theta)$		Normalized single indexed Zernike polynomials
$Z_n^m(r, \theta)$		Normalized double indexed Zernike polynomials
γ		Exponent of the gamma correction
λ	[m]	Wavelength
ϕ	[rad]	Phase of a wave
ρ	$[m^{-1}]$	Wavefront curvature of a spherical wavefront
ρ_{ref}	$[m^{-1}]$	Reference wavefront curvature
ρ_{calc}	$[m^{-1}]$	Calculated wavefront curvature
θ_i	[rad]	Angle of an incident ray
θ_R	[rad]	Angle of a reflected ray
θ_r	[rad]	Angle of a refracted ray

Introduction

The Shack-Hartmann wavefront sensor (SHWS) was developed in the late 1960s by Dr. Roland Shack to improve the images of satellites taken from the earth [1]. Light has to travel through the atmosphere, however, the atmosphere is not a homogeneous environment and has perturbations of refractive index caused by local changes of temperature, pressure and other factors. Therefore, the wavefront becomes aberrated before it reaches the sensor (CCD, CMOS).

To eliminate the phenomenon, Dr. Aden Mienel proposed the idea of measuring the optical transfer function (OTF) of the atmosphere with a Hartmann test, at the same time as the image of the satellite is taken. When the OTF is known, it is possible to partly correct the aberrations. However, it was not possible to cover the aperture of the telescope with a Hartmann screen so Dr. Mienel proposed to include the beam splitter with a Hartmann screen behind the eyepiece. This approach had also several other issues such as the weak intensity of the projected spots and worse accuracy of the spot centroid measurements. Therefore Dr. Roland Shack proposed simple yet powerful innovation by replacing the Hartmann screen with an array of microlenses.

The invention has opened a whole new field and SHWS is being used in various disciplines nowadays. Examples of the applications are adaptive optics, ophthalmology, precise metrology, etc. [2, 3, 4] The sensor is very precise, easy to use and robust to surrounding conditions.

Many companies are offering solutions for SHWS. However, they are often so-called black boxes meaning the manufacturer is usually not providing very deep information about the characteristics of the algorithms or the sensor. This is not optimal for the experimental applications, where it is useful to know the parameters of the reconstruction since they usually need to be varied dramatically based on the task. Another problem is that there is often a need for external calibration. The leading scientific organization TOPTEC was missing the sensor that would provide such variability without sacrificing the high precision of the wavefront reconstruction.

Hence the goal of this thesis is to develop an universal software for the reconstruction of a wavefront using a SHWS with any given parameters. The features should include the calibration routine and provide variability in choosing the reconstruction parameters. The principal limitations and accuracy of the reconstruction should be analyzed using the simulations and also by experimental measurements.

1 Rays and Wavefronts

Light is an electromagnetic wave, that can be according to Maxwell theory described with the so-called wave equation [5, 6]:

$$\nabla^2 U(\mathbf{r}, t) = \frac{1}{v^2} \frac{\partial^2 U(\mathbf{r}, t)}{\partial t^2} \quad (2.1)$$

where $v = \frac{c}{n}$ is the speed of light in a medium with refractive index n , $c = 3 \times 10^8 \text{ ms}^{-1}$ is the speed of light in a vacuum and $U(\mathbf{r}, t)$ is a function characterizing a wave field in space and time t . Every solution of equation 2.1 is a wave, one of them being a monochromatic plane wave in a homogeneous, isotropic medium:

$$U(\mathbf{r}, t) = U_0 e^{j(\mathbf{k}\mathbf{r} - \omega t)} \quad (2.2)$$

where U_0 is the amplitude, ω the angular frequency, f is the frequency, $\mathbf{r}(x, y, z)$ is the position vector, $\mathbf{k} = k\mathbf{s} = k_0 n\mathbf{s}$ is the wave vector parallel to the unit vector \mathbf{s} pointing in the direction of the wave propagation, $k_0 = \frac{2\pi}{\lambda}$ being the wavenumber in a vacuum and λ is the wavelength. The phase of the wave is $\phi(\mathbf{r}) = (\mathbf{k}\mathbf{r} - \omega t)$. We can define surfaces in space with equal $\phi(\mathbf{r})$ as wavefronts.

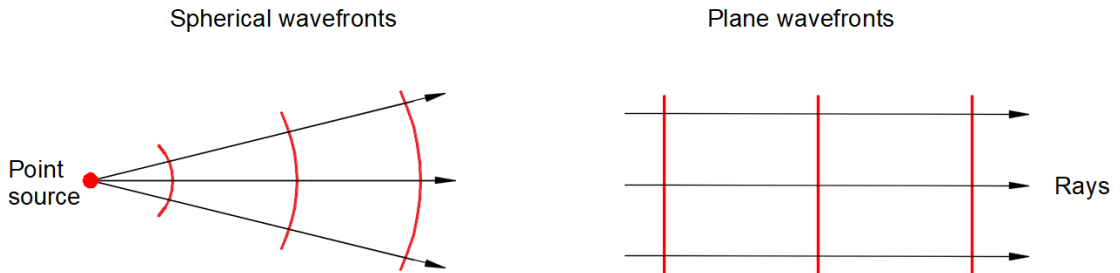


Figure 2.1: Illustration of perfect spherical and plane waves, with rays perpendicular to the wavefronts (surfaces of constant phase).

To describe the phenomena appearing in this thesis, it is sufficient to use the lowest level approximation - ray optics, which is the approximation of scalar wave optics, if we assume that wavelength $\lambda \rightarrow 0$ [7]. To understand the connection between the scalar wave and ray optics, lets imagine that a wave is propagating in the direction of unit vector \mathbf{s} , inside an inhomogeneous medium with a slowly varying refractive index, hence $n(\mathbf{r})$. We assume that the solution of equation 2.1 will take the form [7]:

$$U(\mathbf{r}, t) = U_0 e^{j(k_0 S(\mathbf{r}) - \omega t)} \quad (2.3)$$

where $S(\mathbf{r}) = n(\mathbf{r})\mathbf{s}\mathbf{r}$ is the optical path length (OPL), so-called eikonal. By inserting the form of equation 2.3 into Maxwell equations it is possible to derive the

eikonal equation [5, 7] :

$$(\nabla S)^2 = n(\mathbf{r})^2 \quad (2.4)$$

The wavefront can be now defined as the surface in space with a constant value of eikonal $S(\mathbf{r}) = \text{const.}$, hence constant phase. It can be proven, that gradient of a function is perpendicular to the surfaces of constant value, therefore, ray can be defined as the normal to the wavefront that defines the propagation direction [5, 7].

Equation 2.4 implies that in an isotropic inhomogeneous medium will rays curve in to the areas with higher refractive index, therefore wavefront shape is affected when traveling through the medium. The practical implication of this phenomenon was described in the introduction. When rays travel in a homogeneous and isotropic medium ($n = \text{const.}$), trajectories will be straight lines.

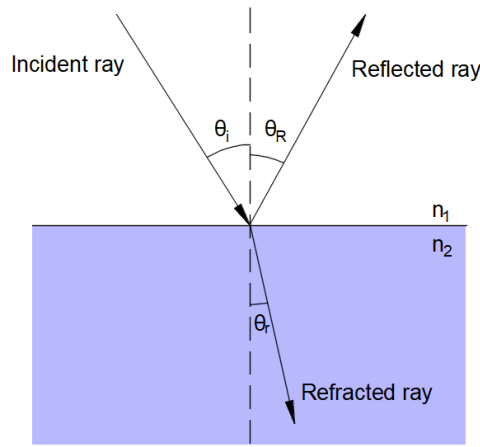


Figure 2.2: Reflection and refraction of the ray incident on to the interface of materials 1 and 2 with different refractive indices n_1 and n_2 respectively ($n_1 < n_2$).

It can be shown with the use of equation 2.4 that the so-called Fermat's principle applies. It states that light traveling between two points takes the path that takes the least time. Furthermore, two fundamental laws of geometrical optics can be derived. First is the law of refraction, so-called Snell's law, that describes the relationship between a ray incident on the interface of two media with different refractive indices and refracted ray [5, 7]:

$$n_1 \sin\theta_i = n_2 \sin\theta_r \quad (2.5)$$

Second is the law of reflection, which states that the angle of incidence θ_i is equal to the angle of reflection θ_R :

$$\theta_i = \theta_R \quad (2.6)$$

1.1 Optical systems

The ideal optical system gathers light from a point source, that radiates perfect spherical waves, and redirects them that they form a single image point [8].

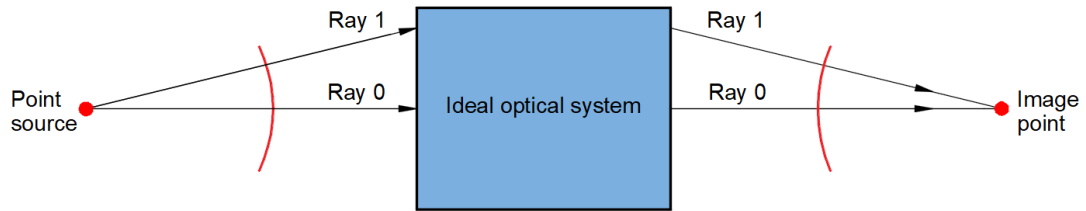


Figure 2.3: The ideal optical system, that gathers light from a point source and focuses it perfectly on to a image point.

Real optical systems work with aberrated wavefronts. The deviation between the wavefront shapes is defined as optical path difference (OPD), which is the difference in the distance that the aberrated wavefront has to travel compared to the perfectly spherical wavefront. This implies that the rays will not converge perfectly into the image point, which leads to a loss in the performance of the system [9].

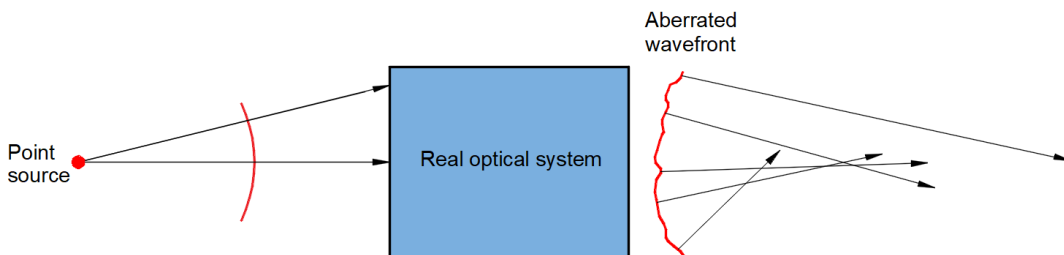


Figure 2.4: Illustration of the aberrated wavefront on the output of a real optical system.

1.2 Zernike polynomials

Let us introduce a function $W(r, \theta)$ that describes the OPD of a wavefront in every point on its specific surface in polar coordinates. This allows us to use the mathematical form of polynomials to describe aberrations of the system. In 1934 Fritz Zernike defined set of so-called Zernike polynomials, which are widely used as wavefront representation for several reasons. They are defined over a unit circle $x^2 + y^2 \leq 1$, which is useful, since the majority of the optical systems have circular pupils.

The most important property is orthonormality, hence orthogonality. Two functions $f(x)$ and $g(x)$ are orthogonal when integration of their dot product is

equal to zero:

$$\int f(x) \cdot g(x) dx = 0 \quad (2.7)$$

To get an idea about orthonormality, imagine a two-dimensional space. Two vectors can form a basis if they are linearly independent, meaning that we can express any given vector in the space using these two basis vectors. An orthonormal basis is a special case of linearly independent vectors when they are also perpendicular to each other and have a unit length such as in the case of the Euclidian plane. If we have a random position vector defined in a plane with an orthonormal basis and subtract one of the basis vectors from the position vector, we do not change the position in terms of the second basis vector.

This implies that each Zernike polynomial describes one specific monochromatic aberration, therefore, we can subtract any given aberration from the wavefront, without affecting the others, hence we can represent a wavefront as [10]:

$$W(r, \theta) = \sum_{n,m} C_n^m Z_n^m(r, \theta) = \sum_{n,m} C_n^m N_{nm} U_n^m(r, \theta) \quad (2.8)$$

where m and n are nonnegative integers, $U_n^m(r, \theta)$ are the polynomials, C_n^m are the coefficients and N_{nm} is the normalization factor, which is defined as:

$$N_{nm} = \sqrt{(2 - \delta_{n,2m})(n+1)} \quad (2.9)$$

where $\delta_{n,2m}$ is the standard Kronecker delta. We can use double index form using polar coordinates $x = r \cos \theta$, $y = r \sin \theta$:

$$U_{nm}(r, \theta) = \begin{cases} R_n^{|n-2m|}(r) \sin(n-2m)\theta, & \text{for } n-2m > 0 \\ R_n^{|n-2m|}(r) \cos(n-2m)\theta, & \text{for } n-2m \leq 0 \end{cases} \quad (2.10)$$

where radial polynomials $R_n^\mu(r)$ are defined as:

$$R_n^\mu(r) = \sum_{k=0}^{\frac{n-\mu}{2}} (-1)^k \frac{(n-k)!}{k! \left(\frac{n-\mu}{2} - k\right)! \left(\frac{n+\mu}{2} - k\right)!} r^{n-2k}; \quad n \geq 0, \quad 0 \leq \mu \leq n, \quad n - \mu \text{ even} \quad (2.11)$$

Note that there is many different indexing schemes, normalizations and conventions in the literature, more information can be found in [10, 11, 12]. In this thesis, the Noll [13] single indexing scheme will be used:

$$j = \frac{n(n+1)}{2} + |m'| + \begin{cases} 0, m' > 0 \wedge n \equiv \{0, 1\} \pmod{4} \\ 0, m' < 0 \wedge n \equiv \{2, 3\} \pmod{4} \\ 1, m' \geq 0 \wedge n \equiv \{2, 3\} \pmod{4} \\ 1, m' \leq 0 \wedge n \equiv \{0, 1\} \pmod{4} \end{cases} \quad (2.12)$$

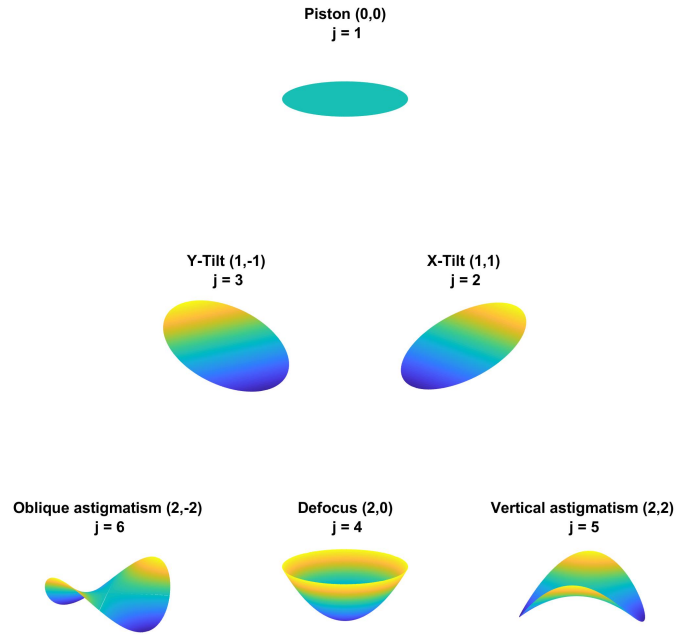


Figure 2.5: Surface plots of first 6 Zernike polynomials with names of classical aberrations, (n - radial order, m - angular frequency), j - Noll single index.

Another practical property of Zernike polynomials is that the root mean square error ($RMSe$) of the wavefront, which is equal to its standard deviation, can be expressed as [11]:

$$RMSe = \sqrt{\sum_{j=4}^J C_j^2} \quad (2.13)$$

The sum starts at $j = 4$ hence piston and both tilts are excluded.

2 Background for Wavefront Sensing

The Hartmann test was invented by the German astronomer Johannes Franz Hartmann at the turn of the twentieth-century [14] as a tool to measure aberrations of mirrors used in telescopes. Let us consider a perfectly spherical mirror and a Hartmann screen with an array of holes in front of it. The mirror will form a perfectly spherical wavefront. We let a point source shine on to the mirror through the Hartmann screen. The light is reflected and forms an image with an array of spots identical to the screen on to the Hartmann plate (Figure 3.6).

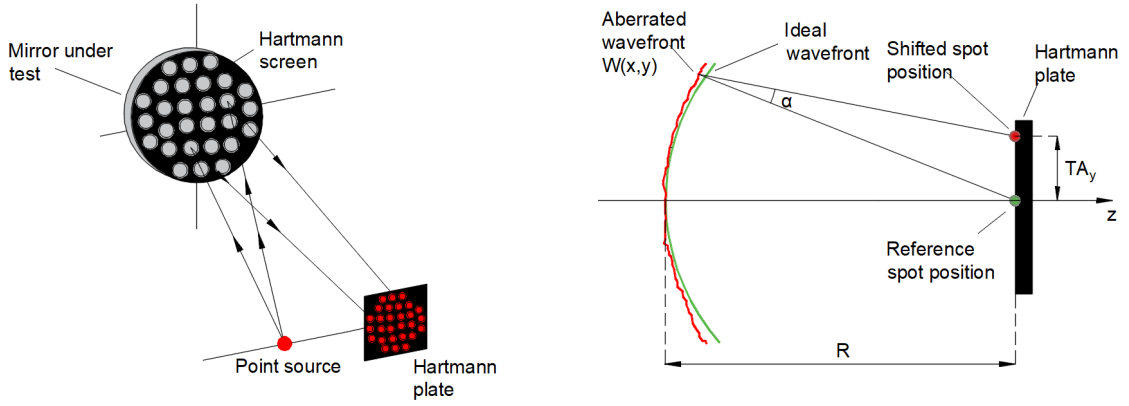


Figure 3.6: Hartmann mirror test arrangement proposed by Johannes Franz Hartmann (left). Illustration of relation between rays and wavefront aberrations (right).

The local slopes of the wavefront will be different from the ideal wavefront when we use an aberrated mirror. This leads to a deviation of the spots from the ideal positions on the Hartmann plate. The relation between the function of the aberrated wavefront $W(x,y)$ and the transverse shifts of the spots in TA_x and TA_y in x and y directions, which represent rays of light traveling from the hole in the Hartmann screen to the spot on the Hartmann plate has been derived by Wayant et. al. [15] as:

$$TA_x = -R \frac{\partial W(x,y)}{\partial x} \quad TA_y = -R \frac{\partial W(x,y)}{\partial y} \quad (3.14)$$

where R is the radius of curvature (RoC) of the reference spherical wavefront. The principle of a SHWS is almost similar to the Hartmann mirror test and it will be described in the following chapter.

2.1 Operating principle of the Shack-Hartmann wavefront sensor

SHWS is used for characterization of a wavefront incident on a microlens array consisting of positive lenses each with equal focal length. Light is focused by the lenses and we can assume that diffraction-limited spots are created on a CCD sensor. When the plane wave is incident on the array the spots will be in a regular grid spaced by the distance between the center of lenses (lens pitch). In the case of an aberrated wavefront, the spots will be shifted in x and y directions by TA_x and TA_y based on a wavefront slope in front of each lens. The area of the lens projected onto the CCD sensor is the so-called region of interest (ROI).

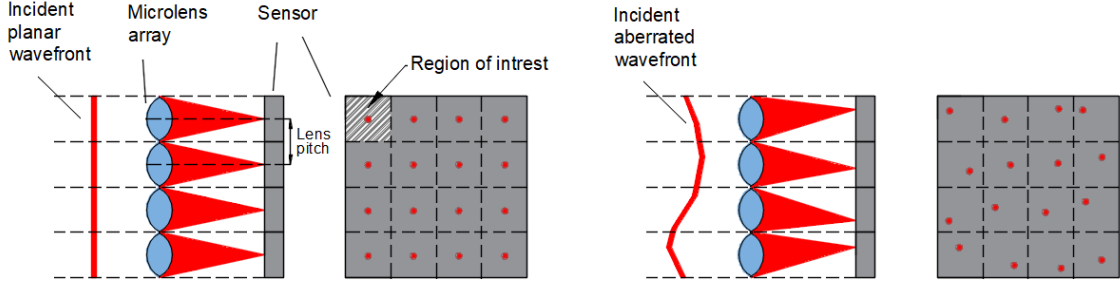


Figure 3.7: Working principle of a Shack-Hartmann sensor. Spots are projected onto a CCD sensor by microlenses. Each spot is in a rectangular ROI. The reference centroid positions are measured using a plane wavefront (left). The aberrated wavefront shifts the spots from the reference positions (right).

The similarity with the Hartmann sensor can be seen, however, in the case of a SHWS the reference wavefront is a perfect plane wave incident parallel to the optical axis of the microlenses, which means, that the slope of the wavefront in front of each microlens is equal to zero. On the other hand, if an aberrated wavefront hits the array the slope will be non-zero and will be directly represented by the shifts of the spots TA_x and TA_y .

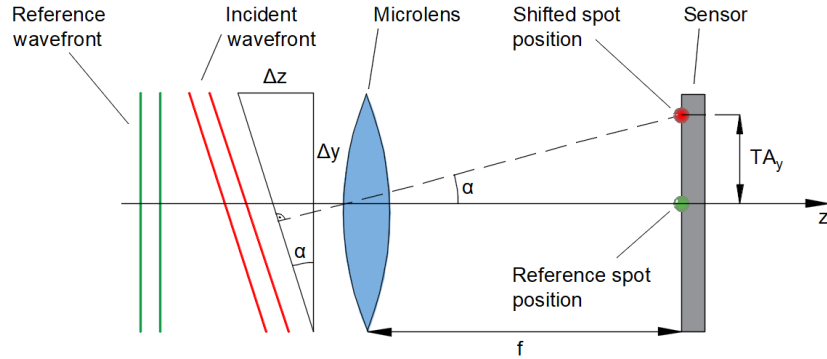


Figure 3.8: The shift of the spot from the reference position, which is caused by the change of the wavefront slope.

A simple and intuitive explanation based on trigonometry is illustrated on figure 3.8. We obtain a geometrical term which describes the slope of the wavefront:

$$\tan(\alpha) = \frac{\Delta z}{\Delta y} = \frac{TA_y}{f} \quad (3.15)$$

where f is the focal length of the microlenses. This leads to almost similar equations as in the case of a Hartmann sensor (equation 3.14). Only difference is

that the radius of curvature is replaced by the focal length:

$$\frac{TA_x}{f} = \frac{\partial W(x, y)}{\partial x} \quad \frac{TA_y}{f} = \frac{\partial W(x, y)}{\partial y} \quad (3.16)$$

These are the basic equations, that describe the relationship between the wavefront slope and the shifts of the spots. They lead to the reconstruction of the entire wavefront. The process will be described in the following chapters. Note, that a detailed derivation of equation 3.16 based on Fourier optics can be found in [3] by Novak et. al.

2.2 Detection of the spot centroids

In order to find the shifts of the spots, it is necessary to determine their centroids. This has to be done with subpixel accuracy if we want to achieve a highly accurate model of the incident wavefront. The problem is, that each lens will create diffracted spot, the so-called Airy disk with a diameter D_{airy} given by [3]:

$$D_{airy} = \frac{2.44\lambda f}{d} \quad (3.17)$$

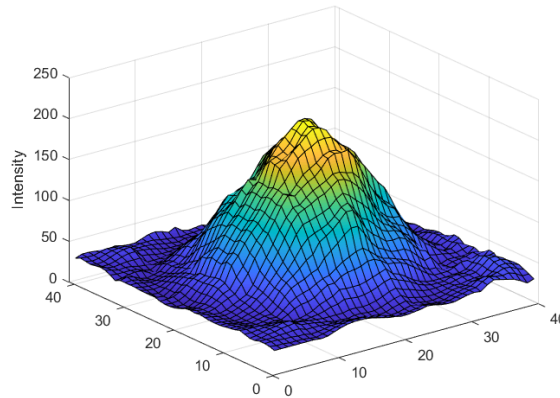


Figure 3.9: Intensity distribution of the diffracted spot imaged on to the CCD sensor.

where d is the microlens diameter. Each microlens can also introduce some aberration, caused by manufacturing imperfection. This means, that each spot will have a complex intensity distribution (Figure 3.9). If we assume, that the image sensor is a grid of pixels with rows and columns with indices row and col respectively, we can determine centroid coordinates \bar{x} and \bar{y} of arbitrary intensity

pattern by finding its first moment (center of gravity - CoG) [3]:

$$\bar{x} = \frac{\sum_{col=0}^{col_{max}} \sum_{row=0}^{row_{max}} I(row, col) s_{pix} col}{\sum_{col=0}^{col_{max}} \sum_{row=0}^{row_{max}} I(row, col)} \quad \bar{y} = \frac{\sum_{col=0}^{col_{max}} \sum_{row=0}^{row_{max}} I(row, col) s_{pix} row}{\sum_{col=0}^{col_{max}} \sum_{row=0}^{row_{max}} I(row, col)} \quad (3.18)$$

where $I(row, col)$ is the measured intensity and s_{pix} is the pixel size.

2.3 Wavefront reconstruction methods

To reconstruct the wavefront, we have to compute the local slopes at the given position c , r on the grid:

$$S_{row,col}^X = \frac{TA_x}{f} = \frac{\bar{x}_{row,col}(ref) - \bar{x}_{row,col}(aberr)}{f} \quad (3.19)$$

$$S_{row,col}^Y = \frac{TA_y}{f} = \frac{\bar{y}_{row,col}(ref) - \bar{y}_{row,col}(aberr)}{f} \quad (3.20)$$

Afterward, it is possible to tackle the reconstruction problem with so-called zonal and modal methods, which are traditionally and widely used and will be described in the following chapters. Note that there are also alternative methods for wavefront reconstruction [16, 17], however, they will not be discussed in this thesis, because they are not implemented in the presented software.

2.3.1 Modal wavefront reconstruction

In the case of the modal reconstruction is a wavefront described as a set of smoothly varying modes [18], in our case, it is represented with a set of Zernike polynomials Z_j :

$$W(x, y) = \sum_{j=0}^J C_j Z_j(x, y) \quad (3.21)$$

where C_j are approximated coefficients of the polynomials. When we substitute in to equation 3.16 we obtain:

$$\frac{TA_x}{f} = \frac{\partial W(x, y)}{\partial x} = \sum_{j=0}^J C_j \frac{\partial Z_j(x, y)}{\partial x} \quad (3.22)$$

$$\frac{TA_y}{f} = \frac{\partial W(x, y)}{\partial y} = \sum_{j=0}^J C_j \frac{\partial Z_j(x, y)}{\partial y} \quad (3.23)$$

which can be written in matrix form as:

$$\mathbf{s} = D\mathbf{c} \quad (3.24)$$

where \mathbf{s} is the column vector of the slopes, D is the matrix containing the partial derivatives of the polynomials and \mathbf{c} is the column vector of the coefficients:

$$\begin{bmatrix} S_{row_1,col_1}^X \\ S_{row_2,col_1}^X \\ \vdots \\ S_{row_{max},col_{max}}^X \\ S_{row_1,col_1}^Y \\ S_{row_2,col_1}^Y \\ \vdots \\ S_{row_{max},col_{max}}^Y \end{bmatrix} = \begin{bmatrix} \frac{\partial Z_1(row_1,col_1)}{\partial x} & \frac{\partial Z_2(row_1,col_1)}{\partial x} & \cdots & \frac{\partial Z_K(row_1,col_1)}{\partial x} \\ \frac{\partial Z_1(row_2,col_1)}{\partial x} & \frac{\partial Z_2(row_2,col_1)}{\partial x} & \cdots & \frac{\partial Z_K(row_2,col_1)}{\partial x} \\ \vdots & \vdots & \cdots & \vdots \\ \frac{\partial Z_1(row_{max},col_{max})}{\partial x} & \frac{\partial Z_2(row_{max},col_{max})}{\partial x} & \cdots & \frac{\partial Z_K(row_{max},col_{max})}{\partial x} \\ \frac{\partial Z_1(row_1,col_1)}{\partial y} & \frac{\partial Z_2(row_1,col_1)}{\partial y} & \cdots & \frac{\partial Z_K(row_1,col_1)}{\partial y} \\ \frac{\partial Z_1(row_2,col_1)}{\partial y} & \frac{\partial Z_2(row_2,col_1)}{\partial y} & \cdots & \frac{\partial Z_K(row_2,col_1)}{\partial y} \\ \vdots & \vdots & \cdots & \vdots \\ \frac{\partial Z_1(row_{max},col_{max})}{\partial y} & \frac{\partial Z_2(row_{max},col_{max})}{\partial y} & \cdots & \frac{\partial Z_K(row_{max},col_{max})}{\partial y} \end{bmatrix} \begin{bmatrix} C_1 \\ C_2 \\ \vdots \\ C_K \end{bmatrix} \quad (3.25)$$

The matrix D is usually a non-square matrix, hence has no inverse. We can use the least squares method to obtain the solution:

$$\mathbf{c} = (D^T D^{-1})^{-1} D^T \mathbf{s} \quad (3.26)$$

However, $D^T D^{-1}$ is usually singular. We have to use a singular value decomposition to obtain a solution [4]. Decomposing matrix D we obtain $D = USV^T$ where S is the diagonal matrix containing the singular values of the matrix D and solution of equation 3.24 is:

$$\mathbf{c} = VS^{-1}U^T \mathbf{s} \quad (3.27)$$

Another way to make sure the equation can be solved with a least squares method, without affecting the result, is to remove the piston row. It is also possible to add a row with zero at the end of vector s and also a row full of ones at the end of matrix D . Both of these methods change the matrix in a way that it is not singular anymore.

2.3.2 Zonal wavefront reconstruction

The term zonal reconstruction refers to the fact, that we determine the wavefront only in local zones. The zones in the case of a Shack-Hartmann sensor are chosen such that they match the microlens array grid [18]. Geometry developed by Southwell [19] is ideal for a Shack-Hartmann sensor because it offers the lowest error propagation compared to other geometries [20]. Therefore, it is implemented in the presented software.

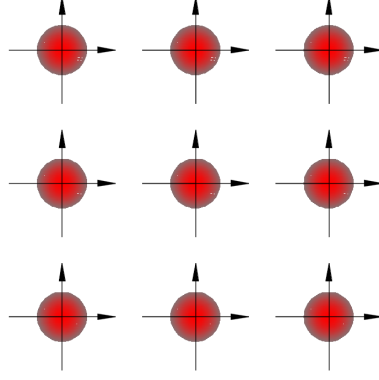


Figure 3.10: Southwell geometry for wavefront estimation scheme. The dots represent phase points (height of the wavefront) and arrows the slope measurements.

Southwell has derived a relation between the local slope measurements and two neighboring phase points with separation length P , which is the lens pitch, as [19]:

$$\frac{S_{col+1,row}^X + S_{row,col}^X}{2} = \frac{W_{col+1,row} - W_{row,col}}{P}; \quad (c = 1, N - 1; \quad r = 1, N) \quad (3.28)$$

$$\frac{S_{col+1,row}^Y + S_{row,col}^Y}{2} = \frac{W_{col+1,row} - W_{row,col}}{P}; \quad (c = 1, N - 1; \quad r = 1, N) \quad (3.29)$$

Equations 3.28 and 3.29 can be solved using the least-squares method. Matrix form can be written as [4, 19]:

$$Cs = Ew \quad (3.30)$$

where \mathbf{s} is the column vector of the slope measurements, \mathbf{w} is the column vector of the incident wavefront phase values and C and E are sparse rectangular matrices. For the reasons stated in chapter 2.3.1 equation 3.30 can be solved with singular value decomposition of matrix $E = USV^T$, obtaining the column vector w with values of wavefront heights:

$$\mathbf{w} = VS^{-1}U^T C\mathbf{s} \quad (3.31)$$

To represent the wavefront obtained by zonal reconstruction with Zernike polynomials, one more computational step is needed. Equation 3.31 can be represented in matrix form as:

$$\mathbf{w} = \mathbf{c}Z \quad (3.32)$$

where \mathbf{c} is the column vector of coefficients containing Zernike coefficients, Z is the matrix containing sampled values of the Zernike coefficients for phase points. Note that column vector w has to contain only values inside the defined circular aperture for reasons explained in chapter 1.2. We can solve the equation with the least squares method [21]:

$$\mathbf{c} = (Z^T Z^{-1})^{-1} Z^T \mathbf{w} \quad (3.33)$$

2.4 Principal limitations of the sensor

It is necessary to have only one spot in each ROI, otherwise, we are not able to link the reference point to the displaced one. The focal length of the microlenses determines by how far is the spot displaced, therefore, the dynamic range but also the sensitivity of the sensor is affected [3, 22]:

$$\left(\frac{\partial W(x, y)}{\partial x}\right)_{max} = \left(\frac{\partial W(x, y)}{\partial y}\right)_{max} = \frac{TA_x^{max}}{f} = \frac{TA_y^{max}}{f} = \frac{D_{airy}}{2f} \quad (3.34)$$

Equation 3.34 tells us that the lower the focal length higher the maximum displacement of the spot hence dynamic range. In other words, the equal slope creates a less displaced spot when the focal length is lower. Hence we can detect higher slopes of the wavefront without having two spots in one ROI.

On the other hand, the sensitivity is affected in the opposite way. The minimum detectable displacement depends on the accuracy of the algorithms for the spot centroids detection. When the focal length is long, a small change in a wavefront gradient causes a relatively big displacement of the spot, which we are able to detect by the algorithms. Therefore, there is always a trade-off between dynamic range and sensitivity. Note that there are specialized algorithms that use spot sorting to increase the dynamic range [21, 23, 24], however, it was not the purpose of this thesis to implement them.

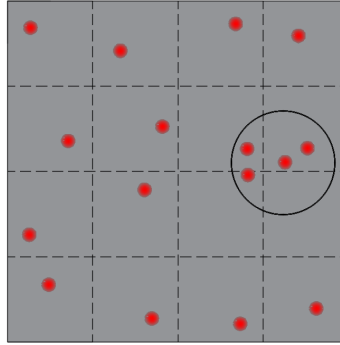


Figure 3.11: We are unable to link the spots inside the circle with the specific ROI hence reference spots. Therefore, it is impossible to reconstruct the wavefront properly with the classical algorithms presented in this thesis.

The microlens array is acting as a low pass filter in terms of spatial resolution. The wavefront is discretized and the aberrations of high spatial frequencies are smoothed out. When the diameter d of the microlenses is smaller, we can fit more of them into the same area, hence the discretization effect is reduced. However, looking at equations 3.34 and 3.17, decreasing the microlens diameter d also decreases the lens pitch P and increases the diameter of an Airy disk D_{airy} , therefore, the dynamic range is reduced. There is again a trade-off between dynamic range and spatial

resolution. More about the design of the SHWS and its limitations can be found in [22, 23].

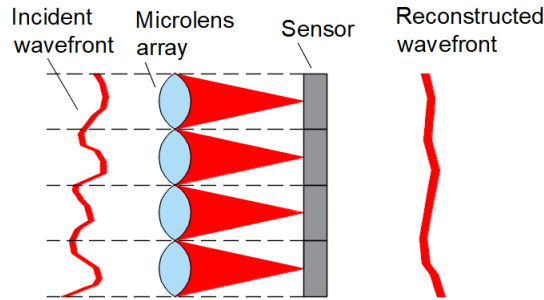


Figure 3.12: Illustration of the smoothing effect of a wavefront with high spatial frequency.

3 Implementation of the Wavefront Reconstruction in MATLAB

The following chapters will outline the principles of the most important algorithms used in the software implementation of the wavefront reconstruction which is the main topic of this thesis. The process will be described step by step and go more deeply into the topics of previous chapters. The software was implemented in MATLAB version R2018b, because it offers several advantages for scientific and engineering projects, due to multiple built-in functions and toolboxes. It is also optimized for matrix operations hence well-written code is efficient and fast.

The structure of the software can be broken down into two steps, we have to determine sensor reference centroids and perform parameter correction first, then we can perform the wavefront reconstruction accurately.

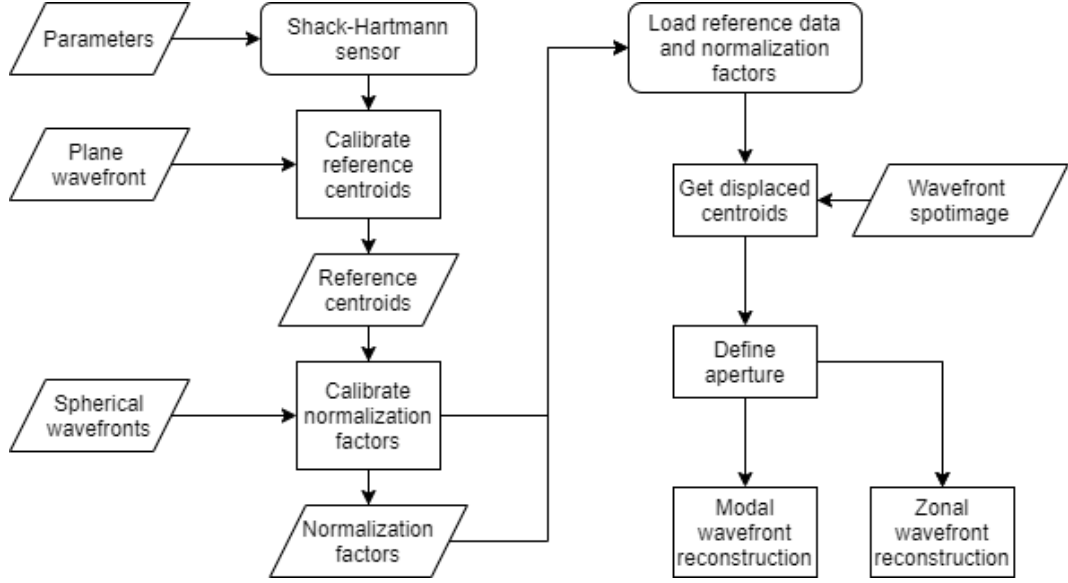


Figure 4.13: Basic structure of the software.

3.1 Algorithms for the detection of the spot centroids

As explained in chapter 2.2 it is necessary to determine the spot centroids with subpixel accuracy. However, the simplest CoG method (equation 3.18) is not accurate enough when the signal-to-noise ratio (SNR) of a spot image is low. The SNR is defined as [25]:

$$SNR = \frac{S_{mean}}{N_{std}} \quad (4.35)$$

where the S_{mean} is the mean intensity value of all pixels. N_{std} is the standard deviation of the intensity value of all pixels and it says how much the overall intensity varies from the S_{mean} , hence it describes the noise. Due to the wide dynamic range the SNR value is often expressed using logarithmic decibel scale:

$$SNR_{db} = 10 \log_{10} SNR \quad [dB] \quad (4.36)$$

SNR is affected by background light, dark noise of the camera sensor and other factors, hence it was necessary to implement algorithms to increase the robustness of the reconstruction. The software allows the user to choose the optimal spot centroids detection algorithm based on his requirements. It will be shown in chapter 4.1.1 that each of the algorithms is useful in different conditions.

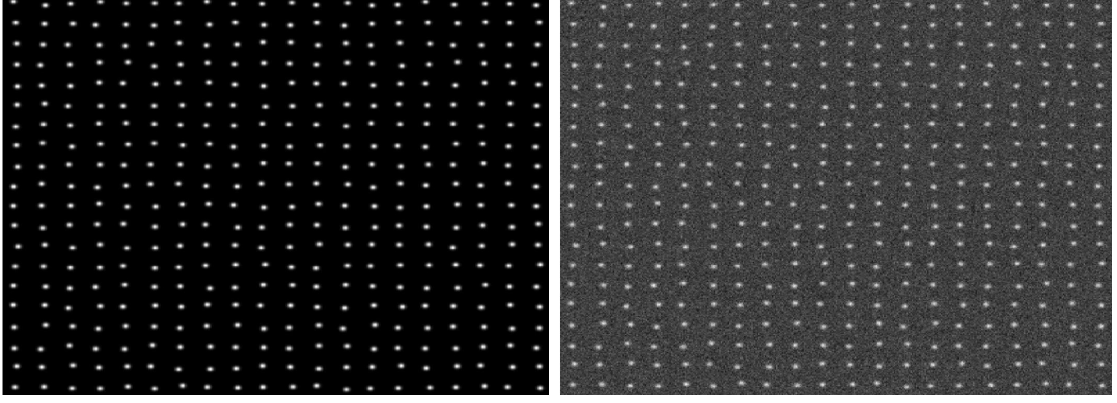


Figure 4.14: Examples of spot images generated with the simulation environment with $SNR_{dB} = 100$ dB (right) and $SNR_{dB} = 20$ dB (left). The spots have perfect Gaussian intensity distribution.

3.1.1 Thresholding

We can reduce the noise by introducing thresholding function $T(row, col)$ which sets the pixel value to zero when its intensity is lower than the threshold level t , therefore:

$$T(row, col) = \begin{cases} 1, & I(row, col) > t \\ 0, & I(row, col) < t \end{cases} \quad (4.37)$$

The equation 3.18 for the CoG calculation becomes:

$$\bar{x} = \frac{\sum_{col=0}^{col_{max}} \sum_{row=0}^{row_{max}} I(row, col) s_{pix} T(row, col) c}{\sum_{col=0}^{col_{max}} \sum_{row=0}^{row_{max}} I(row, col)} \quad (4.38)$$

$$\bar{y} = \frac{\sum_{col=0}^{col_{max}} \sum_{row=0}^{row_{max}} I(row, col) s_{pix} T(row, col) r}{\sum_{col=0}^{col_{max}} \sum_{row=0}^{row_{max}} I(row, col)} \quad (4.39)$$

3.1.2 Gamma correction

Another way to reduce the noise is to use a gamma correction which leads to non-linear relationship between the intensity levels. The corrected intensity value is calculated as:

$$I_{corr}(row, col) = I_{max} \left(\frac{I(row, col)}{I_{max}} \right)^\gamma \quad (4.40)$$

The equation 3.18 for the CoG calculation becomes:

$$\bar{x} = \frac{\sum_{col=0}^{col_{max}} \sum_{row=0}^{row_{max}} I_{corr}(row, col) s_{pix} col}{\sum_{col=0}^{col_{max}} \sum_{row=0}^{row_{max}} I_{corr}(row, col)} \quad (4.41)$$

$$\bar{y} = \frac{\sum_{col=0}^{col_{max}} \sum_{row=0}^{row_{max}} I_{corr}(row, col) s_{pix} row}{\sum_{col=0}^{col_{max}} \sum_{row=0}^{row_{max}} I(row, col)} \quad (4.42)$$

The low intensity pixels become much lower relative to the high intensity ones after the calculation. This means that the noise is reduced and the intensity of the spots is enhanced.

As the value of γ increases, higher the upward-sloping of the function, hence bigger the relative difference between the intensity levels. Experiments and simulations have shown that the optimal value for most of the applications is $\gamma = 2$.

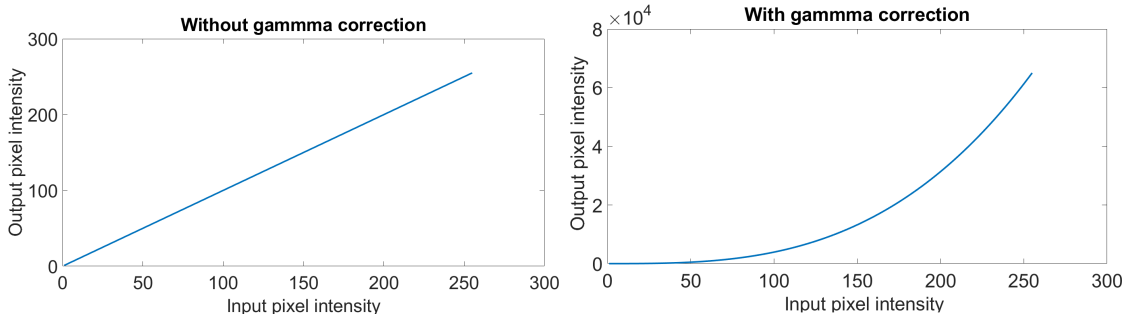


Figure 4.15: The non-linear output of intensity using the gamma correction with $\gamma = 2$.

3.1.3 Windowing

Windowing is a simple technique used for improvement of the accuracy of the CoG methods. We define a rectangular window with a certain width, with center at the pixel of maximum intensity, and set the pixels outside the rectangle to zero [21].

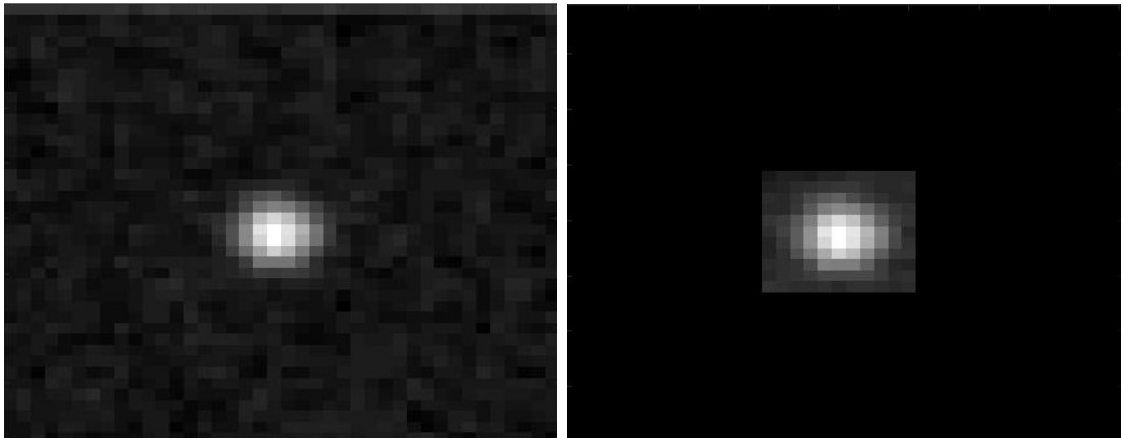


Figure 4.16: Example of windowing used in a noisy ROI.

3.1.4 Correlation

Both of the algorithms above are based on the modification of the CoG method. The correlation algorithm uses a different principle. It calculates a cross-correlation function between a model of the light spot and the sub-image, corresponding to the ROI. The best matching pixel is found.

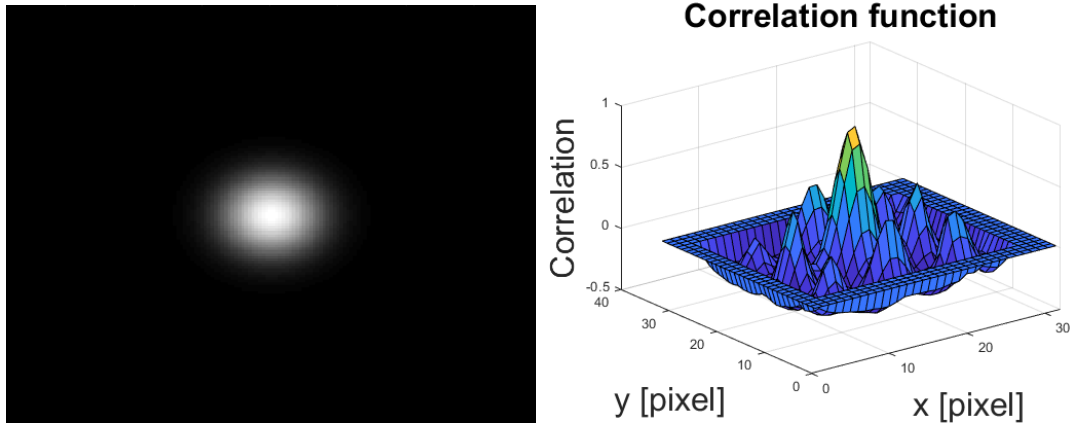


Figure 4.17: In the left there is a template of the perfectly gaussian spot used to find the centroid of the noisy image on the left side in figure 4.16. We can see that the correlation function has its peak in the middle, where the spot in figure 4.16 is located.

To get the sub-pixel accuracy it is necessary to apply a parabolic or gaussian interpolation using the neighbouring pixels. A detailed explanation can be found in the literature [21, 26, 27].

3.2 Calibration of the reference centroids

In order to measure the wavefront shape, it is necessary to know the equally spaced reference positions of the centroids, which are generated by a planar wavefront, as stated in chapter 2.1. Theoretically, it is possible to generate a perfect plane wave incident perpendicular to the optical axis of the microlenses by for example taking a single-mode fiber and placing it into the focus of the convex lens.

In reality, the reference centroids will not be equally spaced because the wavefront will be deformed by the fiber and lens imperfections, perturbations of a refractive index, or by having the fiber not precisely in the focus. Another problem is, that the centroiding algorithms work only with a certain precision. Therefore, the calibration process that compensates for the problems mentioned above was implemented.

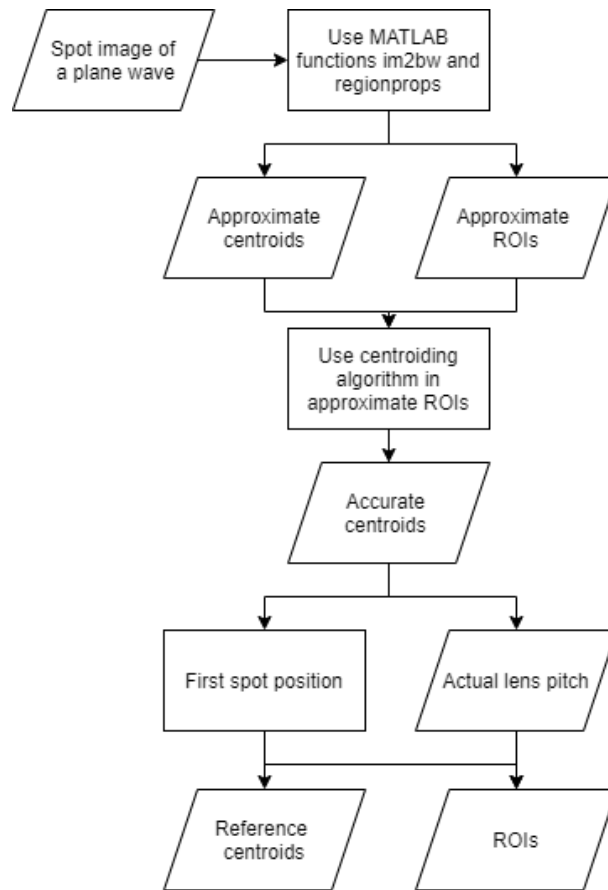


Figure 4.18: Logic of the reference spot position algorithm calibration.

First, the position of the centroids is approximated by analyzing a spot image, generated by a close-to planar wavefront, using the MATLAB functions for thresholding and centroiding gives us approximate centroids. Approximate ROIs are computed based on the size of microlenses, which is known as a manufacturing parameter of a sensor (figure 3.7). Afterward, the centroiding algorithms are used in the approximate ROIs for higher accuracy of the centroids detection.

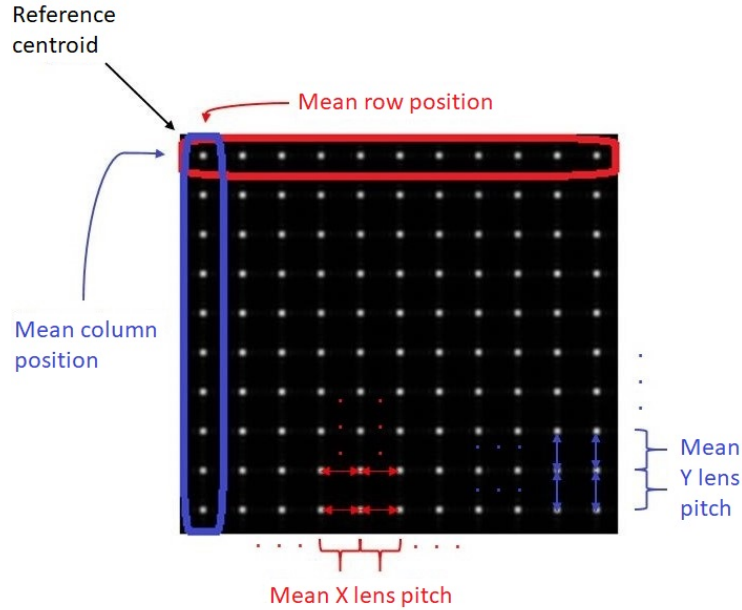


Figure 4.19: Illustration of the reference calibration process.

To simulate behavior of a perfectly plane wavefront, the x and y position of the first reference centroid is calculated by taking the mean centroid position of all spots in the first row and column. Afterward, a mean value of all distances between neighboring centroids in x and y directions is taken, hence mean lens pitch. We add the x and y mean lens pitch values to the position of the reference spot and generate create two new centroid positions in x and y directions. We repeat the process by adding the mean lens pitch values to the new spots until the spot image with equally spaced centroids in x and y directions is generated. The error caused by averaging the values is neglectable, compared to the accuracy of the reconstruction algorithms.

It is necessary to use wavefront as close to perfect plane as possible, therefore, wavefront generated by He-Ne laser in QED's ASI(Q) interferometer with the reference lens diameter of 550 mm was used. The field of view of used Shack-Hartmann sensor with the resolution 1024x1024 is 6 x 6 mm, hence only the small area of the generated wavefront has been analyzed, therefore, we can assume that the RMS_e is close to zero. The complete characterization of the sensor can be found in chapter 4.2.

3.3 Calibration of the normalization factors

Experiments have shown, that the reconstruction wavefront algorithms are behaving differently than expected. It was observed while reconstructing the spherical wavefront with known RoC, that they work properly only when we introduce the normalization factors N_{modal} and N_{zonal} into the calculations. In the

case of modal reconstruction equations 3.22 and 3.23 become:

$$\frac{TA_x}{f} N_{modal} = \frac{\partial W(x, y)}{\partial x} = \sum_{j=0}^J C_j \frac{\partial Z_j(x, y)}{\partial x} \quad (4.43)$$

$$\frac{TA_y}{f} N_{modal} = \frac{\partial W(x, y)}{\partial y} = \sum_{j=0}^J C_j \frac{\partial Z_j(x, y)}{\partial y} \quad (4.44)$$

For the zonal reconstruction, the vector \mathbf{w} in equation 3.31 has to be modified:

$$\mathbf{w}_{normalized} = \frac{\mathbf{w}}{N_{zonal}} \quad (4.45)$$

The normalization factors do not have equal values and in the case of modal routine it is linearly changing with aperture diameter as illustrated in figure 4.20.

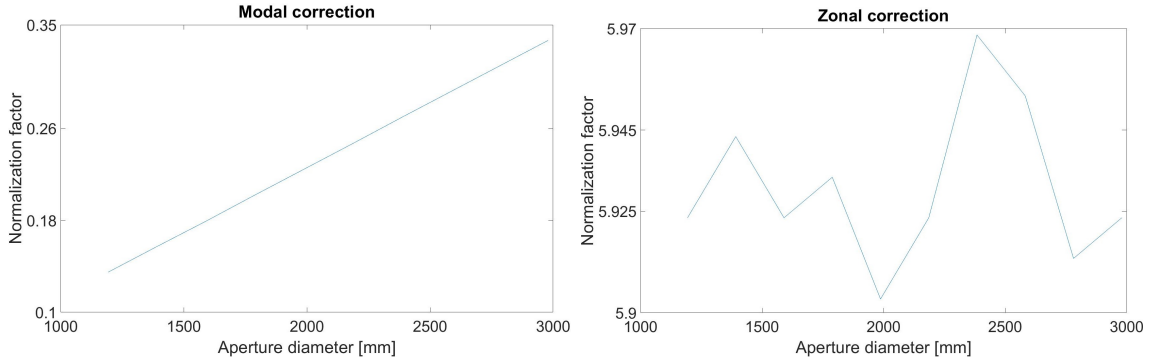


Figure 4.20: The illustration of the normalization factor dependence on the aperture size. The data were obtained by measuring a spherical wavefront with known RoC. The way of obtaining the normalization coefficient is explained further in this chapter.

Even though extensive research, no explanation of these phenomena has been found in the literature. Further mathematical analysis of the algorithms has to be done to find the explanation.

To overcome the problem we introduce one more calibration routine. The idea behind it is based on the literature [28, 29, 30], where the actual parameters of the sensor, such as focal length or pixel size, are determined. These parameters are affected by manufacturing errors and knowing them accurately increases the accuracy of the sensor.

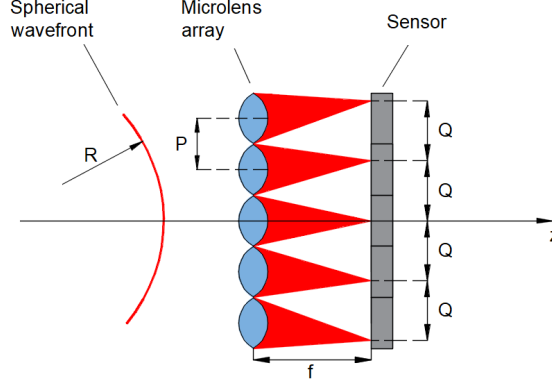


Figure 4.21: Spots created by perfectly spherical wavefront.

This is done by measuring multiple almost perfectly spherical wavefronts, generated by a single-mode fiber, in different distances from the sensor. Note that ρ is so-called wavefront curvature and it can be calculated using the radius of curvature R as:

$$\rho = \frac{1}{R} \quad (4.46)$$

It is obvious that longer the spherical wavefronts travels, lower the ρ . When it reaches the sensor it creates a regular grid of spots with separation distance Q , which is constant for specific range and therefore the wavefront can be approximated by a parabola. Note that lower the ρ the distance Q between the spots gets shorter. If the spherical wavefront travels far enough, due to the divergence and because only a small area of it is analyzed, the wavefront will become almost planar.

When we know the Q , lens pitch P and focal length f , it is possible to calculate the wavefront curvature as:

$$\rho_{calc} = \left(\frac{Q}{P} - 1\right) \frac{1}{f} \quad (4.47)$$

However, we do not know the exact values of f and P and it is impossible to measure the distance from the single-mode fiber to the sensor accurately enough. Therefore, we create a reference mark on the sensor and measure the distance, in other words RoC, R_{ref} from the single-mode fiber to the mark and save the spot image. Afterward, we move the sensor away from the fiber, which changes the RoC hence Q , and we repeat the process.

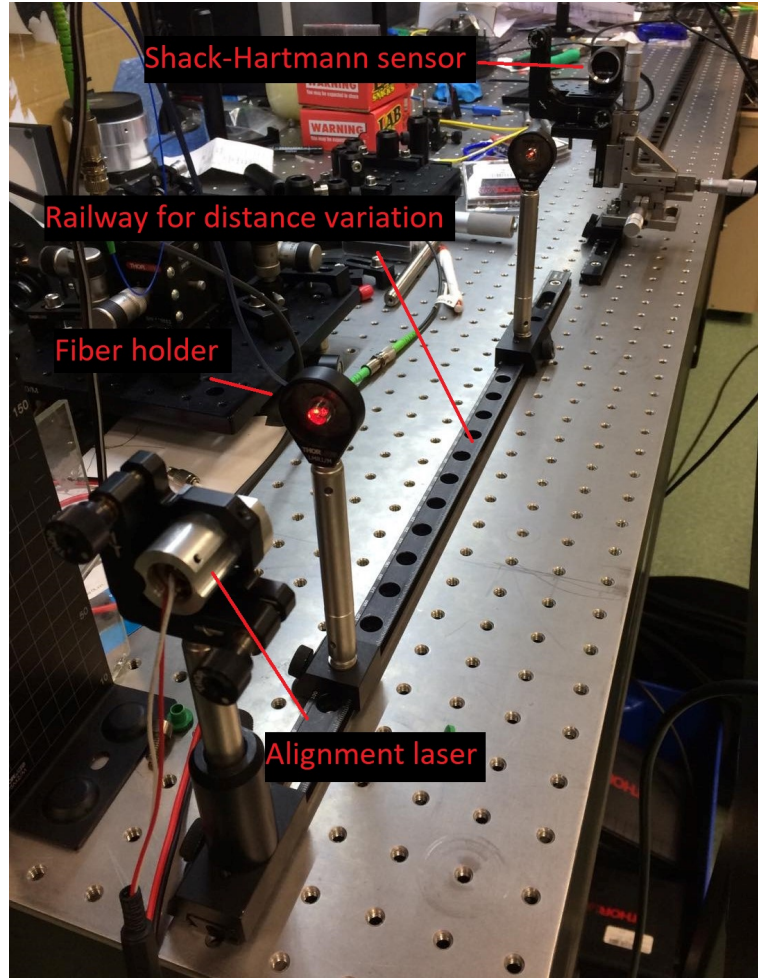


Figure 4.22: Photo of the calibration process.

This gives us multiple values of ρ_{calc} and ρ_{ref} . We calculate $\delta\rho = \rho_{ref} - \rho_{calc}$, plot the data and fit them with a second-order polynomial. It is possible to get the values of δR , δf and δs_{pix} from the fitted coefficients using the equation 4.48, which has the form of the second-order polynomial.

$$\delta\rho = \rho_{ref}^2 \delta R - \rho_{ref} \frac{\delta f}{f} - \frac{1}{f} \left(\frac{\delta P}{P} - \frac{\delta s_{pix}}{s_{pix}} \right) \quad (4.48)$$

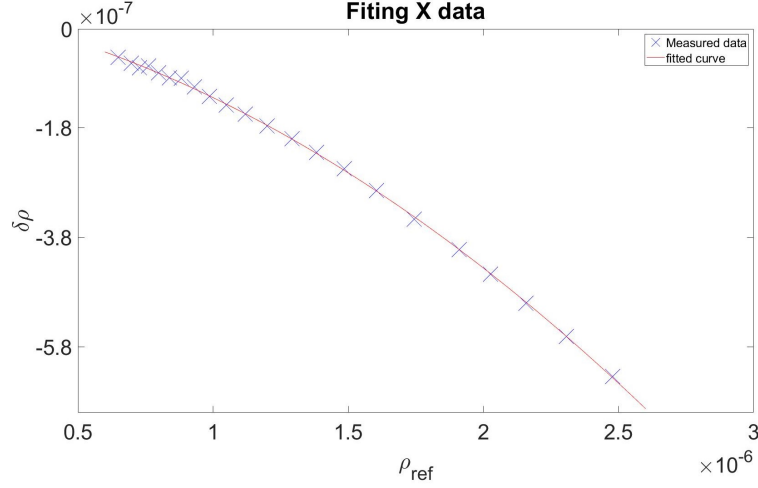


Figure 4.23: Set of measurements of the spherical wavefronts with different radii and the fit of the second-order polynomial.

For the calibration routine, presented in this thesis, it is not necessary to correct for the pixel size or focal length because the correction is included in the normalization factors. When we know the exact value of the RoC of the spherical wavefront, it is possible to find the N_{modal} and N_{zonal} for different aperture diameters D_{aper} by calculating the value of the fourth Zernike spherical coefficient, which is directly connected to the RoC by [31]:

$$C_4 = \frac{D_{\text{aper}}}{8\sqrt{3}R} \quad (4.49)$$

We can use merit functions to find such values of N_{modal} and N_{zonal} that the reconstructed value of the coefficient corresponds to the one calculated using the equation 4.49. Because the N_{modal} is changing linearly with aperture, we fit the data with a first-degree polynomial to get the coefficients of the polynomial, which can be used later for the calculation of N_{modal} for every possible aperture diameter. On the other hand, the N_{zonal} oscillates around one number hence we take the mean to get the final value for all aperture diameters.

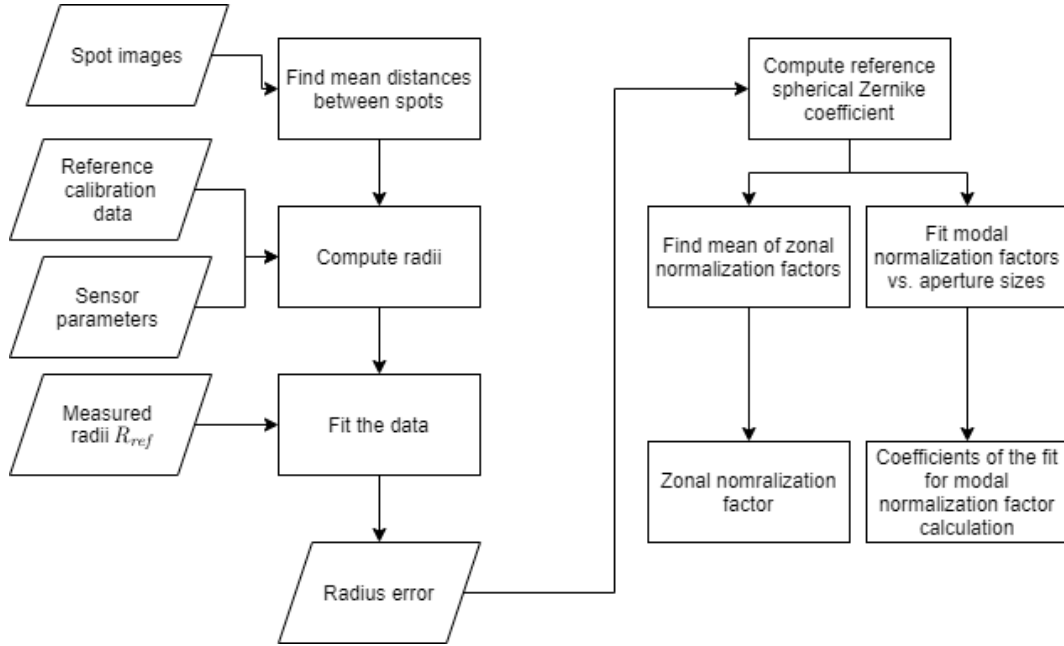


Figure 4.24: Logic of the algorithm for normalization factor calibration.

3.4 Algorithms for the wavefront fitting

With the sensor calibrated by both of the routines, we are able to reconstruct the wavefront using a modal or zonal method. The outputs of both presented fitting algorithms are the Zernike coefficients because of the advantages they provide as explained in chapter 1.2. First, it is necessary to define a circular aperture with a certain diameter and change the coordinate system to polar normalized on unit disk for calculations with Zernike polynomials. User is also allowed to define the orientation of the xyz axis, such as swapping x and y or changing the positive direction of z , which can be useful when the sensor is rotated in space.

3.4.1 Modal fitting routine

As explained in chapter 2.3.1 it is necessary to calculate the derivatives of the Zernike polynomials. It is not recommended to use explicit expressions due to increasing cancellation error. This can be solved by using recurrence relations between the polynomials to calculate the values of higher orders derivatives. For this reason, the robust and stable algorithm presented in [10] is used in the software.

The derivatives are calculated in the x and y coordinates of the reference centroids given by calibration procedure, hence in case the aperture diameter does not change, the computation of all the steps above is done only once. This means that we can effectively reconstruct the wavefront in real-time because the following routine is not time-consuming and we can loop it as illustrated in figure 4.25. The routine includes analysis of the spot image of the distorted wavefront, calculation of the wavefront slopes and using least squares fit to get the Zernike coefficients.

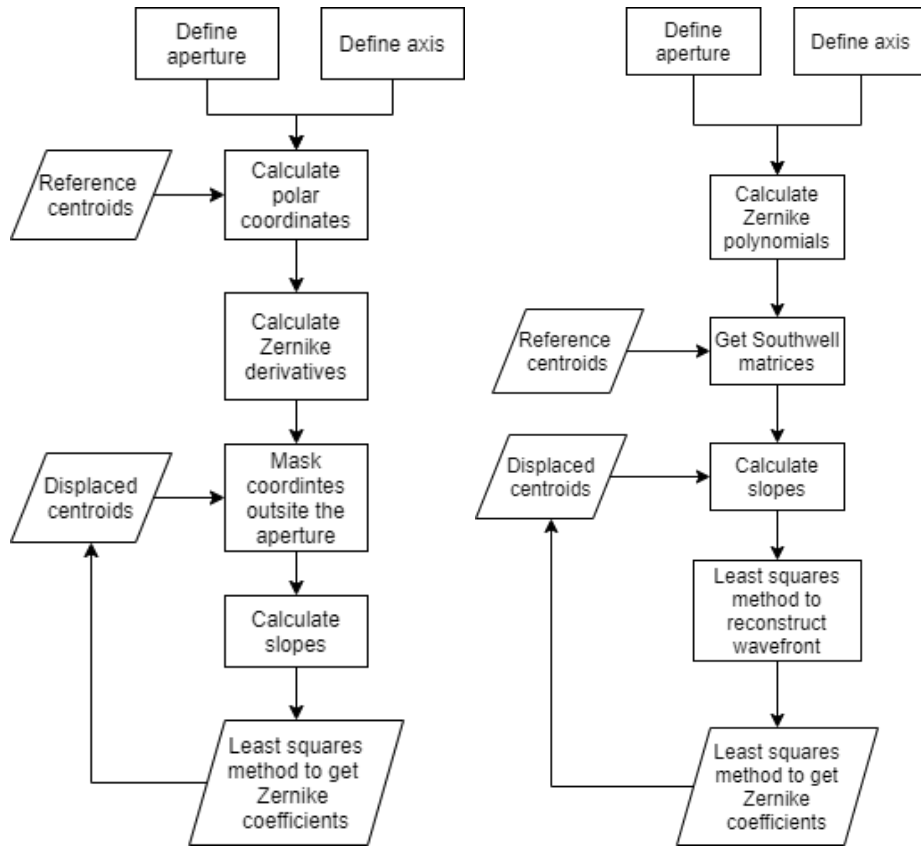


Figure 4.25: Logic of the routine for modal (left) and zonal (right) fitting algorithms. It is possible to loop the part of the fitting and reconstruct the wavefront in real-time if the aperture diameter does not change.

3.4.2 Zonal fitting routine

Zonal fitting requires us to calculate the Southwell matrix using x and y coordinates of the reference centroids. The function `getSouthwellMatrix.m` presented in [21] is utilized for this purpose. The wavefront is reconstructed over the whole spot image by the least squares fit of the slopes and Southwell matrices. Then we calculate the values of Zernike polynomials inside a defined aperture, utilizing the function [32] available in MATLAB Central File Exchange, and by using the least squares fit we get the coefficients, as explained in chapter 2.3.2. It is possible to loop the part of the routine again for a real-time reconstruction.

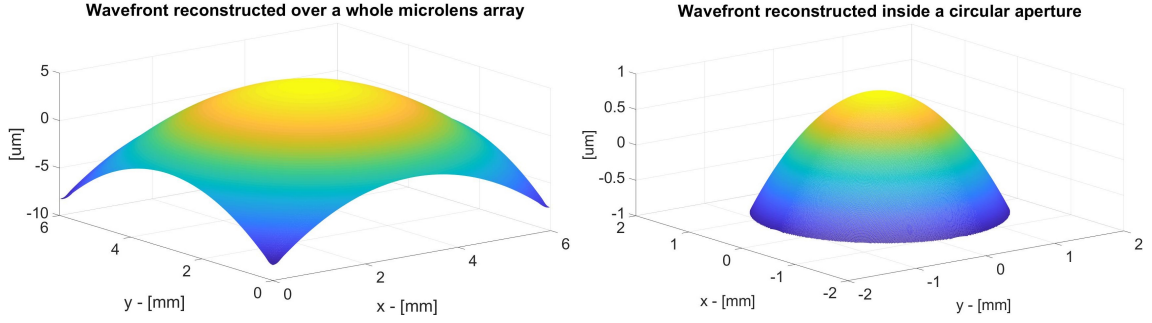


Figure 4.26: Wavefront reconstructed over a whole microlens array and the same wavefront reconstructed inside a 3 mm aperture in diameter using a least squares fit of Zernike polynomials.

4 Analysis of the Algorithms

The following chapters present the analysis of the software in terms of time effectiveness and accuracy via simulation environment and real-world measurements, which are compared with the socertified commercial software by Thorlabs using the WFS30-7AR sensor [31]. The Zernike coefficients reconstructed by Thorlabs software were saved and visualized in MATLAB for an easier comparassion of the results.

4.1 Simulation environment

The simulation environment was developed as the part of this thesis for the further analysis of the algorithm. It takes a set of Zernike polynomial coefficients as an input and generates a corresponding spot image. This is done by reversing the process of the wavefront reconstruction. First, we compute the derivatives of a wavefront characterized by input coefficients inside a defined aperture. Using equations 3.22 we can compute the TA_x and TA_y and simulate the corresponding spot image.

The generated spots have perfect Gaussian intensity distribution. This is done using function `customgauss.m` available in MATLAB Central File Exchange [33]. Analyzing various simulated spot images and performing the reconstruction gives us an idea about the accuracy of the algorithms.

4.1.1 Comparison of the algorithms for the detection of spot centroids via simulation

The accuracy of spot centroid detection algorithms was tested by calculating the absolute difference between the reference centroids and the detected ones for simulated spot images with different SNRs. The generated images had a resolution of 400x400 pixels. The number of generated spots is 400.

The absolute error is the sum of absolute values of differences between the known generated centroid positions and the detected ones. It is expressed in a pixel unit. The SNR of the image is controlled by the MATLAB function `awgn()` which adds a Gaussian noise to the image based on the input, which is a scalar value of SNR_{dB} , which has been calculated using the equation 4.36.

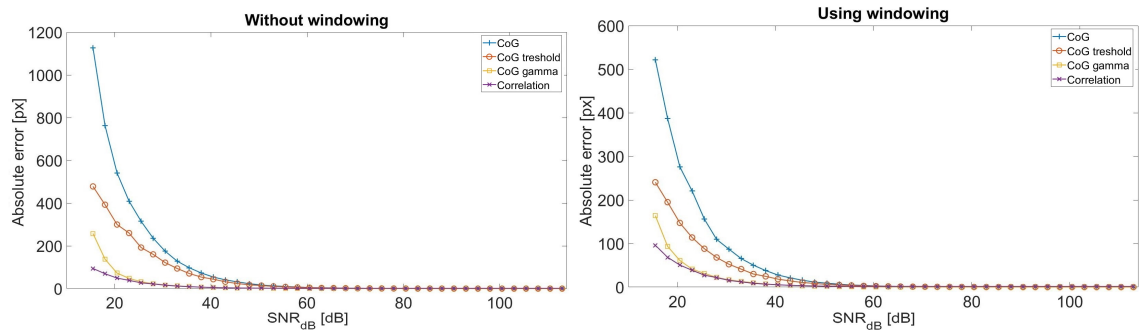


Figure 5.27: Comparison of the algorithms for the detection of spot centroids without and with windowing in terms of absolute error for different values of SNR_{dB} .

We can see in figure 5.27 that all of the methods work perfectly when the SNR is large enough. Even though thresholding improves the simple CoG algorithm, both of them start to fall off relatively soon. The gamma correction and correlation start to introduce error for much lower SNR, than two of the previous methods, and they are even up until the $SNR_{dB} \approx 20$ dB where the gamma correction falls off. To get the idea, the spot image with $SNR_{dB} = 20$ dB can be seen in figure 4.14.

The correlation algorithm is best in terms of accuracy and beneficial for situations where the strong background illumination is present while measuring. Windowing significantly improves the accuracy of CoG algorithms as we can see if we compare pictures in the figure 5.27, on the other hand, it is not surprising that the correlation algorithm is not affected by it.

To compare the algorithms in terms of time efficiency we analyzed 1640 ROIs and measured the time it takes to find the centroids:

Table 5.3: Time efficiency of the centroiding algorithms after analyzing 1640 ROIs.

Algorithm	Time [s]
Simple CoG	0.048
Thresholding	0.096
Gamma correction	0.091
Gamma correction + windowing	0.146
Correlation	1.729

The CoG algorithms are very time efficient compared to the correlation method, however, windowing prolongs the time taken approx. 1.6x. In the majority of the situations in a lab is the SNR_{dB} much higher than 20 dB, therefore, it is recommended to use the gamma correction algorithm with windowing which

allows us to reconstruct the wavefront in real-time with approx. 4 fps assuming the equal number of spots. In situations with very low SNR, or when the time of the reconstruction is not an issue, it is recommended to use the correlation algorithm.

4.1.2 Comparison of the algorithms for wavefront fitting via simulation

To get the idea of the noise introduced only by the modal and zonal fitting algorithms, without being affected by centroiding noise, 10 000 different spot images were generated via simulation and reconstructed.

We were mostly interested in the fitting accuracy of the first fourteen Zernike coefficients. Hence the reference inputs of the simulation were created in such a way, that the first fourteen coefficients are always predominant, coefficients from the fourteenth to twenty-second are all present but lower and coefficients left up until sixty-sixth one are mostly zero, however, few of them are randomly present to simulate a noise introduced by variations in the refractive index.

Difference between the reference C_j^{ref} , which are the coefficients used as an input for the simulation of the spot images, and the fitted coefficients C_j^{fit} of each reconstruction for both of the fitting algorithms were calculated and expressed in terms of RMS_{diff} :

$$RMS_{diff} = \sqrt{\sum_{C_j^{interval}} (C_j^{ref} - C_j^{fit})^2} \quad (5.50)$$

The mean RMS_{diff} of all 10 000 simulations was computed afterward for different sum intervals:

Table 5.4: The RMS_{diff} computed from the difference between the input coefficients and the fitted ones.

C_j interval	Modal RMS_{diff} [nm]	Zonal RMS_{diff} [nm]
$4 \leq j \leq 14$	8.729	16.300
$4 \leq j \leq 66$	13.041	18.520
$2 \leq j \leq 3$	18.427	13.919

The fit of the first fourteen coefficients excluding piston and tilts is almost twice more accurate for modal routine compared to zonal. When we analyze results up until sixty-sixth coefficient, we can see that the RMS_{diff} is larger, even though modal fitting is affected more than zonal it is still more precise. Therefore, the modal fitting seems to be superior to the zonal one. This can be caused by the calibration routine presented in chapter 3.3, where we take only the mean of the zonal normalization factor. More experiments need to be done to increase the accuracy of the zonal fitting.

On the other hand, the zonal routine is more accurate in tilt fitting. This can be caused by the fact, that the modal routine works with derivatives of Zernike polynomials, which are not orthogonal, therefore, the coupling between the coefficients can occur [34].

Note that the $RMS_{e_{diff}}$ values can not be taken as absolute error values of the algorithms, because they slightly change with aperture size, hence with the number of spots inside. In our case, the aperture including 812 spots was analyzed.

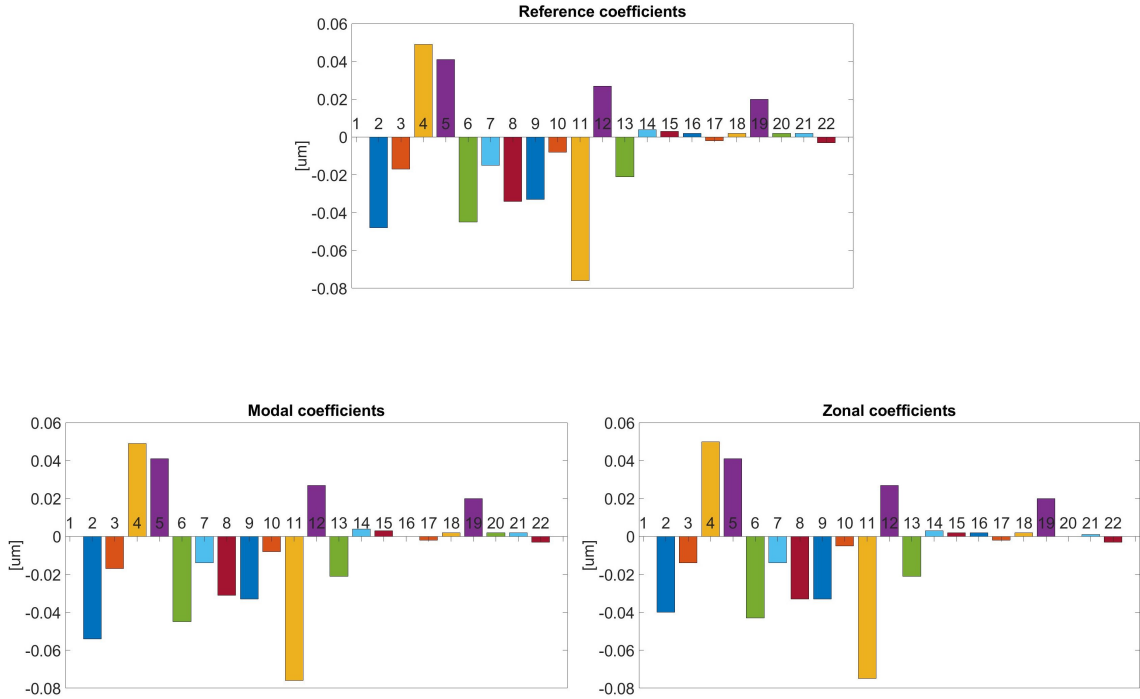


Figure 5.28: Example of a reference and reconstructed coefficients used in simulations.

The reconstruction time of a single wavefront is:

Table 5.5: Time efficiency of the fitting algorithms.

Algorithm	Time [s]
Modal	0.008
Zonal	0.248

The ineffectiveness of the zonal algorithm is caused by the least squares fit of Southwell matrices and slopes, which takes around three-quarters of the time spent. The results lead to the conclusion that the modal fitting is superior to the zonal one in terms of accuracy and speed.

4.2 Comparison of the presented reconstruction software with the commercial software

In order to test the accuracy and noise of the modal and zonal algorithms in real-world condition, we reconstruct almost perfectly planar, spherical and also various

wavefronts. The results are compared with the Thorlabs commercial software that uses calibration data obtained by an unknown method and also uses unknown fitting algorithm.

The sensor (WFS30-7AR) by Thorlabs was used for the reconstructions [31]:

Table 5.6: Specifications of the wavefront sensor used and hardware limitations of the wavefront reconstruction.

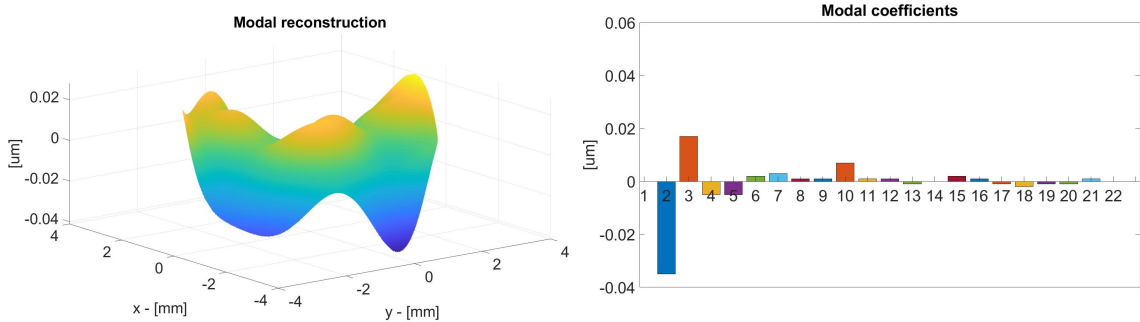
- 1) Resolution is software-changeable, hence the number of used microlenses also differs based on it. In our case resolution of 1024x1024 pixels was used.
- 2) Thorlabs documentation states that accuracy was tested by measuring a spherical wavefront with known RoC generated by a single-mode fiber using a HeNe laser ($\lambda = 633 \text{ nm}$). Accuracy is measured using the commercial software.

Hardware parameters			
Microlenses		Camera	
Focal length	5.6 mm	Sensor	CMOS
Lens pitch	0.15 mm	Resolution ¹⁾	1936 x 1216
Array size	11.5 x 7.5 mm	Pixel size	0.00583 mm
Lens size	0.146 mm		
Number of microlenses	73 x 45		
Limitations of the wavefront reconstruction			
Wavefront accuracy ²⁾		$RMS_e = \lambda/40 = 15.83 \text{ nm}$	

Note that for practical reasons, presented figures contain only first twenty-two Zernike coefficients, but the RMS_e is calculated from fourth to sixty-sixth Zernike coefficient. In every presented chapter a single spot image, that characterizes the wavefront, is taken and analyzed using modal, zonal and Thorlabs reconstruction algorithms. The difference in results is compared.

4.2.1 Reconstruction of the plane wavefront

The close-to planar wavefront generated by ASI(Q) interferometer is used again. We presume, that the wavefront aberrations should be close to zero for reasons explained in chapter 3.2, hence the reconstructed Zernike coefficients should be also close to zero. The accuracy will be affected by the noise introduced by centroiding, fitting algorithms and also by the hardware imperfections of the sensor, such as microlens array aberrations. The aperture diameter was set to 6 mm.



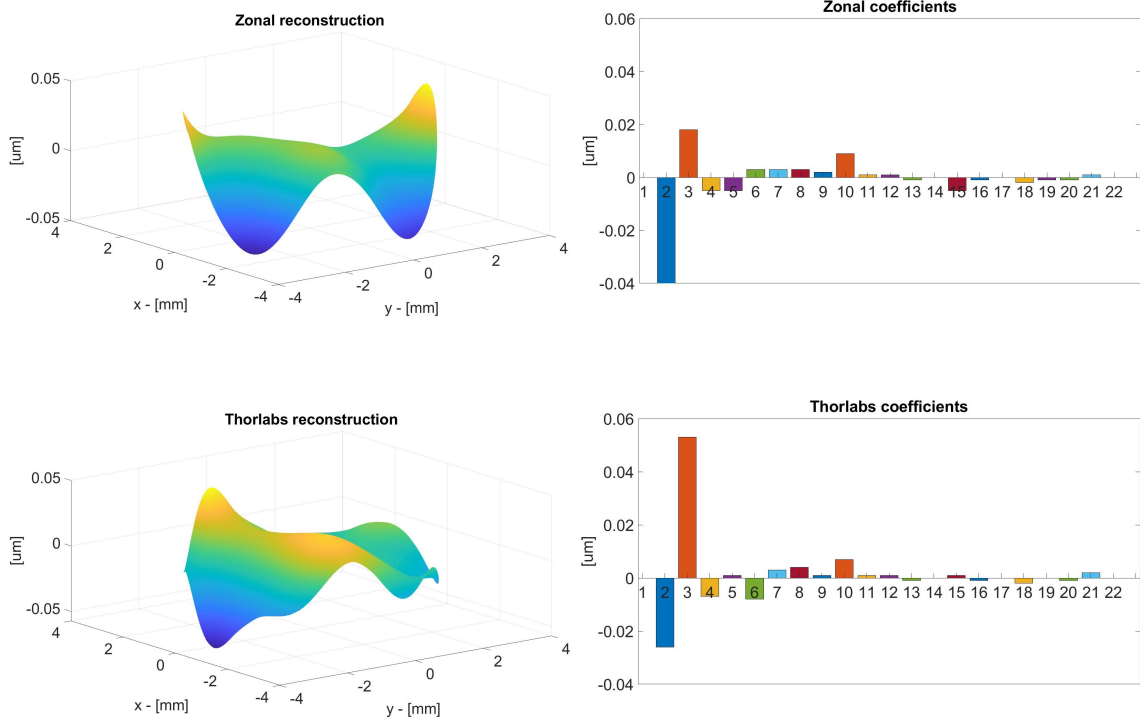


Figure 5.29: Results of the almost perfectly plane wavefront reconstruction.

The difference in reference centroids can also have a major effect on the difference in tilts, which can be seen in figure 5.29 when looking at the values of C_2 and C_3 . The modal reconstruction is again superior to zonal, which correlates with the results of the simulations, and it even seems to be slightly better than the Thorlabs reconstruction.

Table 5.7: The $RMSe$, hence the noise of the algorithms used to reconstruct almost perfectly plane wavefront.

Algorithm	$RMSe$ [nm]
Modal	13.304
Zonal	15.199
Thorlabs	14.353

4.2.2 Reconstruction of the spherical wavefront

The spherical wavefront with known RoC was generated by a single-mode fiber, therefore, we can assume that all of the aberrations except the defocus are close to zero. To test the noise again, we calculate the $RMSe$ without the defocus coefficient C_4 , hence starting the sum at $j = 5$ in equation 2.13. The defocus coefficient was equal for all of the reconstruction routines and it corresponded with the known RoC, hence it did not affect the $RMSe$ calculation. The aperture diameter was set to 3.5 mm.

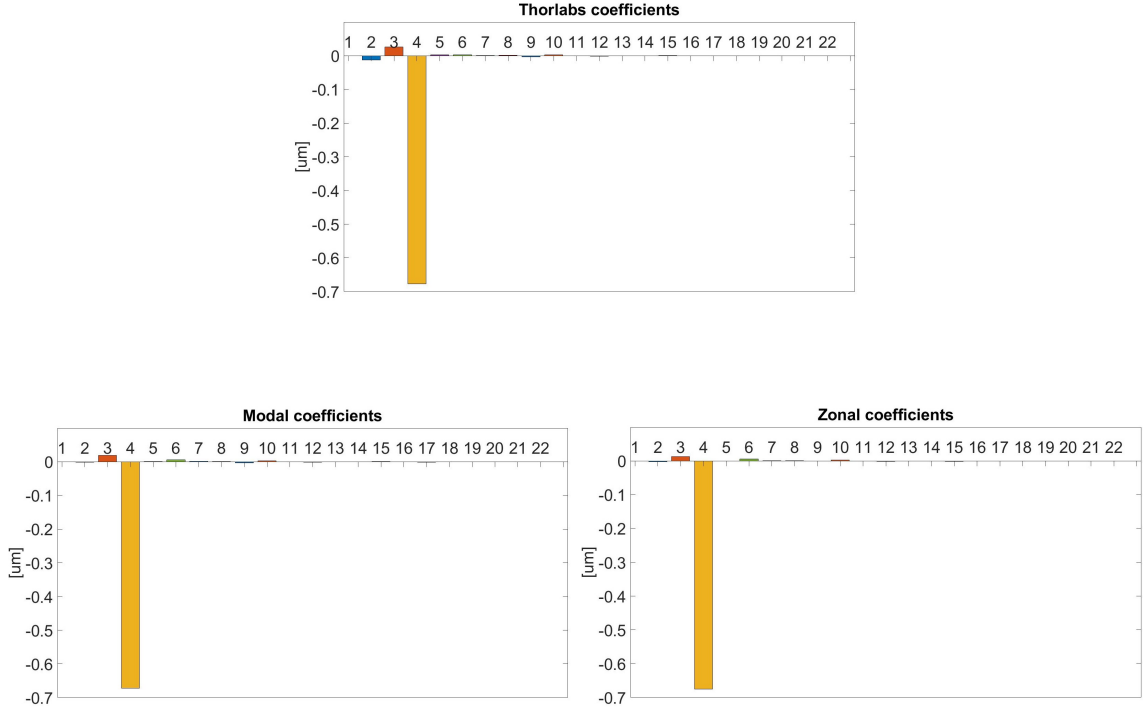


Figure 5.30: Reconstructed Zernike coefficients of the almost perfectly spherical wavefront.

The total $RMSe$ is significantly lower compared to the reconstruction of a plane wavefront in the previous chapter. This is caused by the smaller diameter of the aperture. The relative difference in the $RMSe$ follows the same trend, hence the modal reconstruction is superior to zonal and even Thorlabs reconstructions. The difference in tilt is probably again caused by the difference in reference.

Table 5.8: The $RMSe$, hence the noise of the algorithms used to reconstruct almost perfectly spherical wavefront.

Algorithm	$RMSe$ [nm]
Modal	6.083
Zonal	7.000
Thorlabs	6.633

4.2.3 Reconstruction of the wavefront A

The following chapter presents the reconstructions of various wavefronts A and B generated by the experimental optical system which can be seen in figure 6.36. The aperture diameter was set to be equal as in the previous chapter - 3.5 mm.

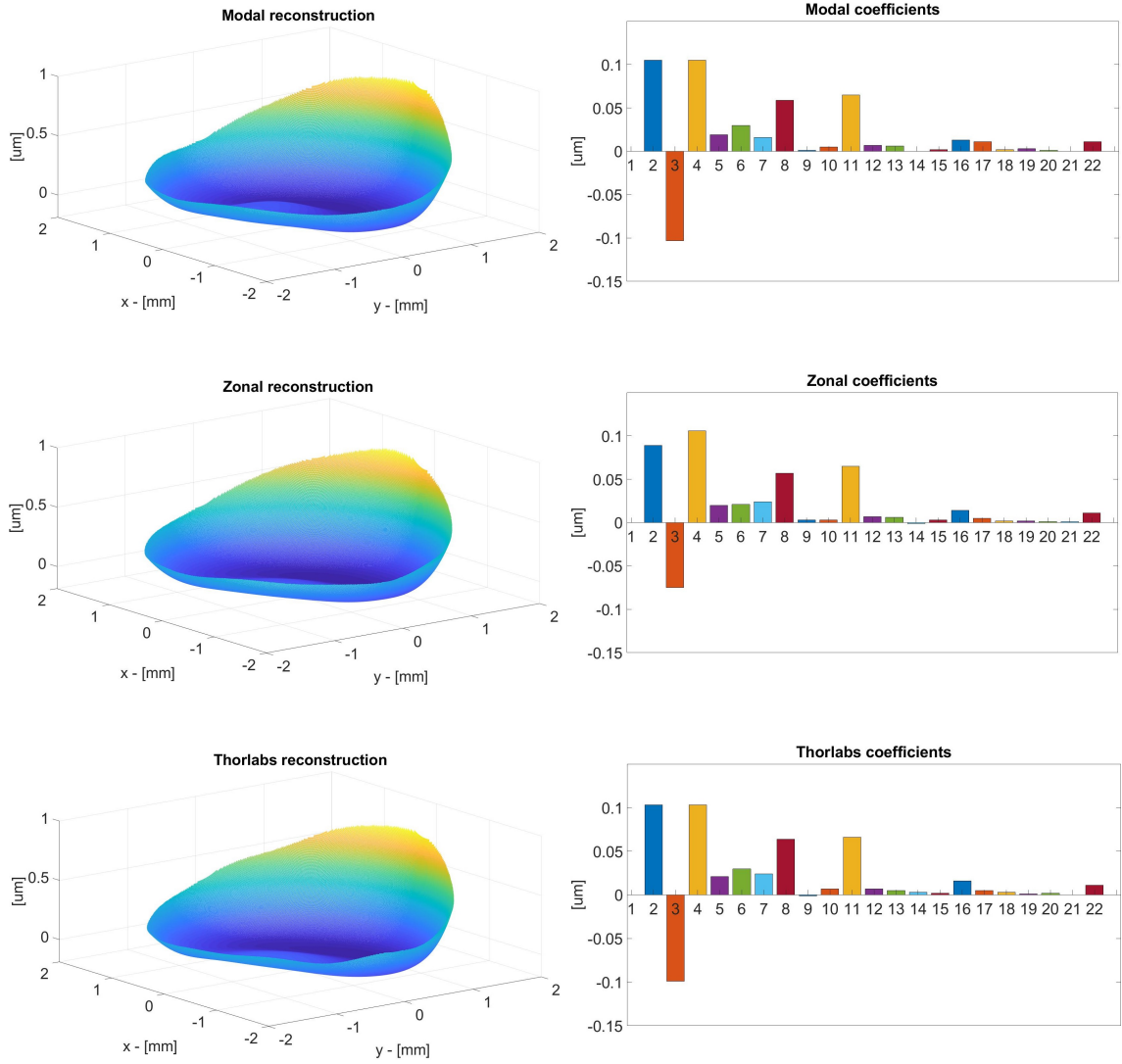


Figure 5.31: Reconstruction of the wavefront A generated by a experimental optical system.

The modal and zonal reconstructions were again compared to the commercial software by calculating the difference in Zernike coefficients and then computing the $RMSe_{diff}$, however, now we calculate the difference between the reconstruction algorithms, therefore in equation 5.50 we replace the variables C_j^{ref} and C_j^{ft} with values of the coefficients obtained by the fitting algorithms. The interval of the coefficients used for the calculaton of the sum is $4 \leq j \leq 66$.

Table 5.9: The $RMSe_{diff}$ of the algorithms calculated from the difference of the fitted coefficients when reconstructing wavefront A.

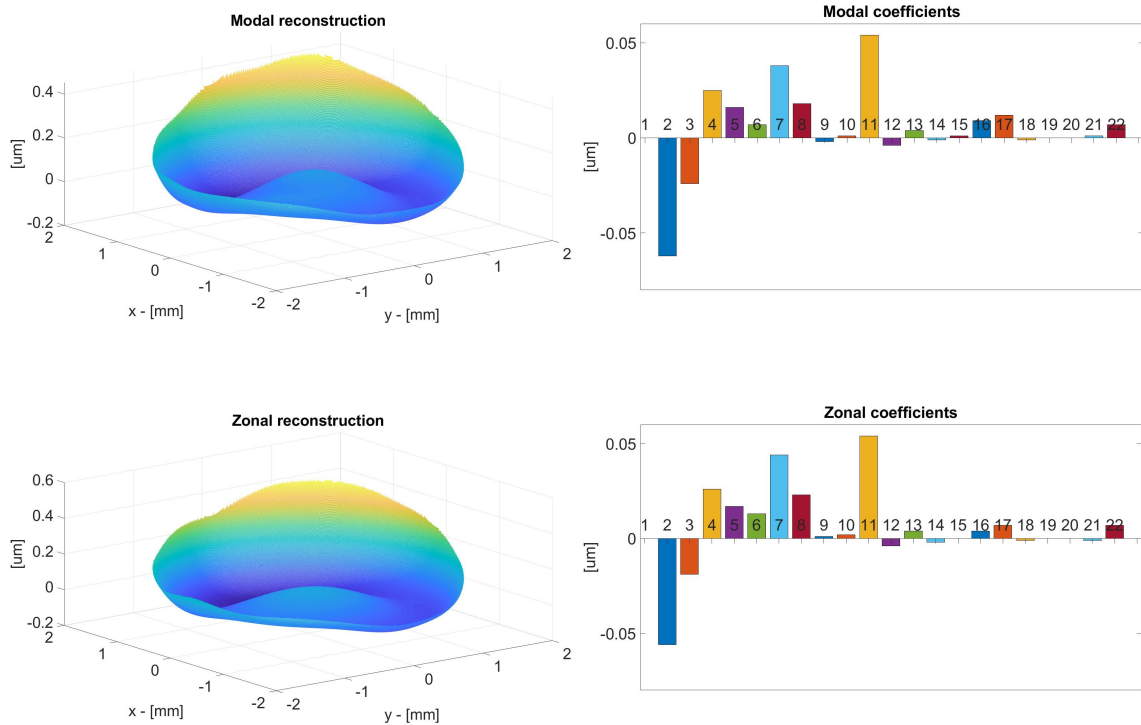
Algorithms	$RMSe_{diff}$ [nm]
Thorlabs - Modal	16.643
Thorlabs - Zonal	16.031
Modal - Zonal	16.673

The $RMSe_{diff}$ between the algorithms is higher than the $RMSe$, in other words, noise of the reconstruction of the spherical wavefront with the same aperture size, that has been analyzed in the previous chapter. This points to the fact, that when if there is more than one dominant aberration present in the wavefront, the accuracy of the reconstruction is worse.

Note that the difference in results between the presented algorithms and the commercial one can be up to a certain degree caused by slightly different size and position of the aperture. Other factors that can affect this are the different reference data or centroid detection methods. However, the important fact is that the relative contribution of Zernike coefficients is almost similar for each reconstruction algorithm.

4.2.4 Reconstruction of the wavefront B

The wavefront B was again generated by the optical system described in chapter 5. Different aberrations than in the previous chapter were purposefully introduced.



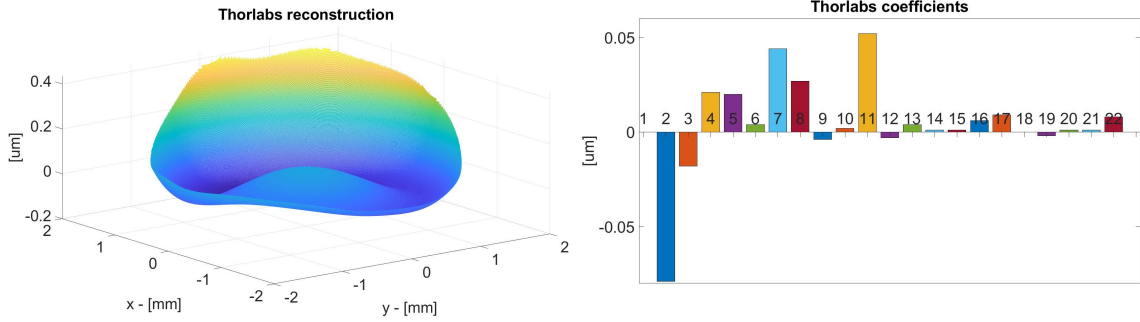


Figure 5.32: Reconstruction of the wavefront B generated by the experimental optical system with induced defocus.

The $RMSe_{diff}$ difference between the algorithms is slightly different, however, close to the values of the reconstruction of the wavefront A. The relative contribution of the Zernike coefficients is again almost similar for each reconstruction algorithm.

Table 5.10: The $RMSe_{diff}$ of the algorithms calculated from the difference of the fitted coefficients when reconstructing wavefront B.

Algorithms	$RMSe_{diff}$ [nm]
Thorlabs - Modal	17.321
Thorlabs - Zonal	15.165
Modal - Zonal	15.460

It was observed by measuring almost perfectly planar and spherical wavefronts, that the modal reconstruction is superior in terms of noise to the zonal and Thorlabs routines. The simulations in chapter 4.1.2 showed that the modal routine is more accurate than the zonal reconstruction with first 14 Zernike coefficients pre-dominantly present and even when we reconstruct all of the 66 coefficients.

It is not obvious, whether is the modal reconstruction superior to the Thorlabs reconstruction algorithm because the exact properties of measured wavefronts are not known. However, by analyzing the results we can say, that the presented software is a solid alternative to the commercial one.

5 Application of the Algorithm for Alignment of the Complex Optical System

When we consider an optical system with multiple optical elements, it is crucial to align all of them properly to minimize the aberrations, otherwise, the overall performance of the system will be degraded. Consider a perfectly aligned optical system in Fig. 6.33, the input and output of the system is a plane wave.

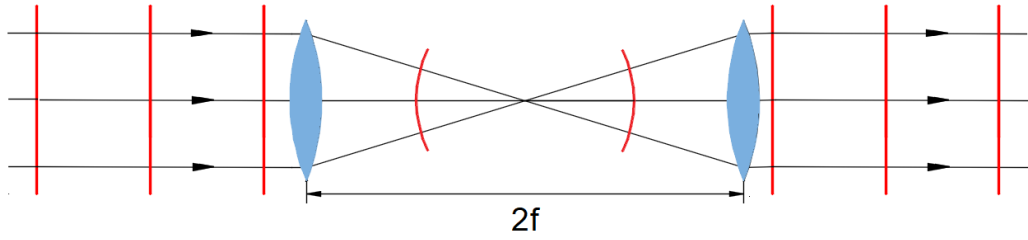


Figure 6.33: Perfectly aligned optical system.

On the other hand, if the lenses are misaligned (Fig. 6.34) the output wavefront is aberrated, therefore the image is distorted and the performance of the system is degraded. The shape of the wavefront can be measured using a SHWS. Based on the aberrations present, it is possible to use the so-called sensitivity matrices to map the link between the misalignments and Zernike coefficients. It is not purpose of this thesis to present the detailed principle, more information can be found in [35].

Note that the complex sensitivity matrix algorithms, that were used for the alignment, were not programmed by the author of this thesis. Author took part in this project by generating a .NET library of the presented SHWS software using the MATLAB Compiler SDK, by programming a part of the application used for the alignment in C# and assisiting when performing the experiments.

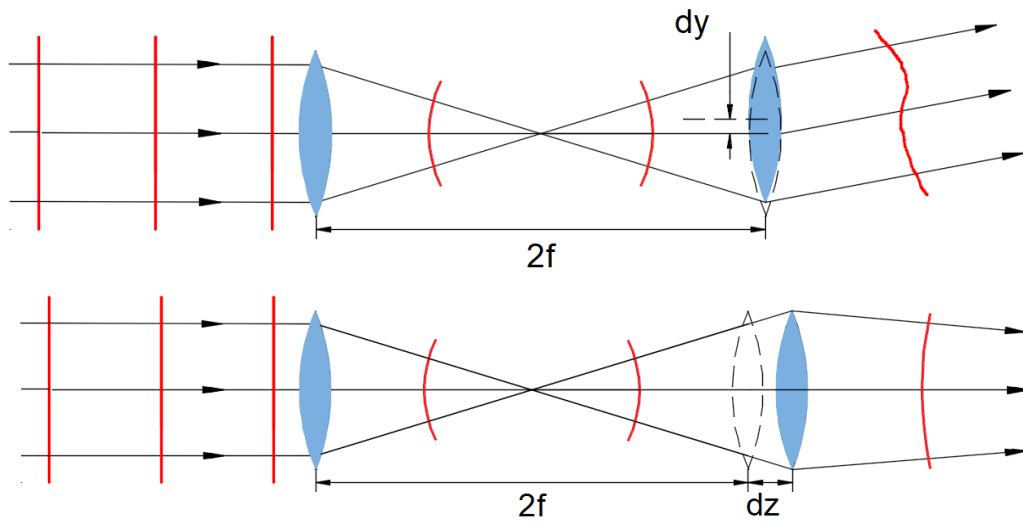


Figure 6.34: Examples of misaligned optical systems - decenter (top) and defocus (bottom).

5.1 Description of the adjusted complex optical system

To test the principle of the alignment with the use of SHWS, the experimental optical system was designed which we can see in figure 6.35. The components are motorized so it is possible to introduce a defined misalignment. The single mode

fiber a) can move in x direction, biconvex lens b) can move in x and y directions, biconcave lens d) in z direction and SHWS e) in x direction.

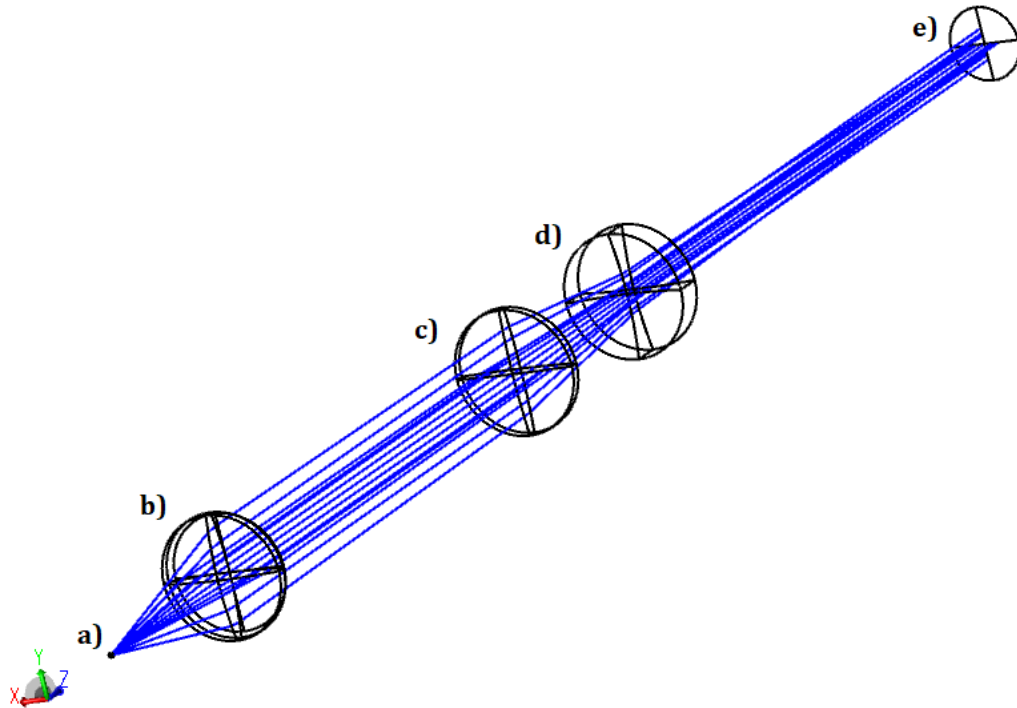


Figure 6.35: The model of the experimental multi-lens optical system generated in Zemax software used for the testing of the alignment algorithms. a) Single mode fiber, b) Biconvex lens, c) Biconvex lens, d) Biconcave lens, e) Shack-Hartmann sensor.

The adjustment algorithm uses information about the wavefront obtained from the Zemax model of the system and information about the wavefront shape reconstructed with SHWS. These are then analyzed using sensitivity matrices.

5.2 .NET library for C# application

There was a need to develop an application that can read raw spot images in real time using the SHWS from Thorlabs and processes them with the presented MATLAB software for a wavefront reconstruction. It was also necessary to control the motors that are moving the lenses in the experimental optical system to introduce a defined misalignment.

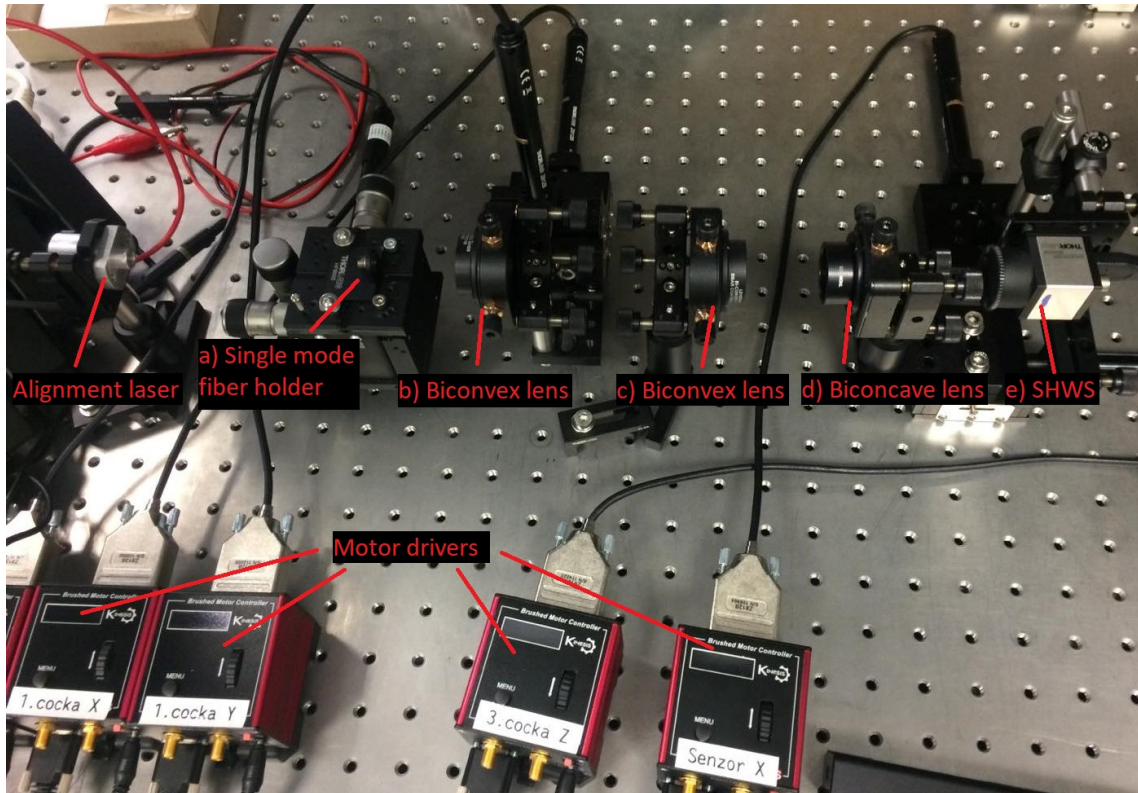


Figure 6.36: Photo of the experimental multi-lens complex optical system.

Thorlabs provides .NET libraries that can be used to connect and control their devices. Hence we decided to develop a C# application which controls the SHWS, the motors and also reconstructs a wavefront using the presetned MATLAB software. Therefore a .NET library of the wavefront reconstruction software was generated using the MATLAB Compiler SDK. The application provides functionality of all three libraries and it can be used as a tool for the alignment of the experimental optical system.

Note, that the raw MATLAB code is used to analyze a single spot image. The C# application allows user to reconstruct a wavefront in a real time.

5.3 Alignment of the complex optical system

When the system was modeled the wavefront on the output of the system can be seen on figure 6.37. The most dominant one is the spherical aberration which is manifested by C_{11} - primary spherical aberration. It is introduced by the nature of the lenses in the system and can not be compensated for without the use of advanced methods of optical design.

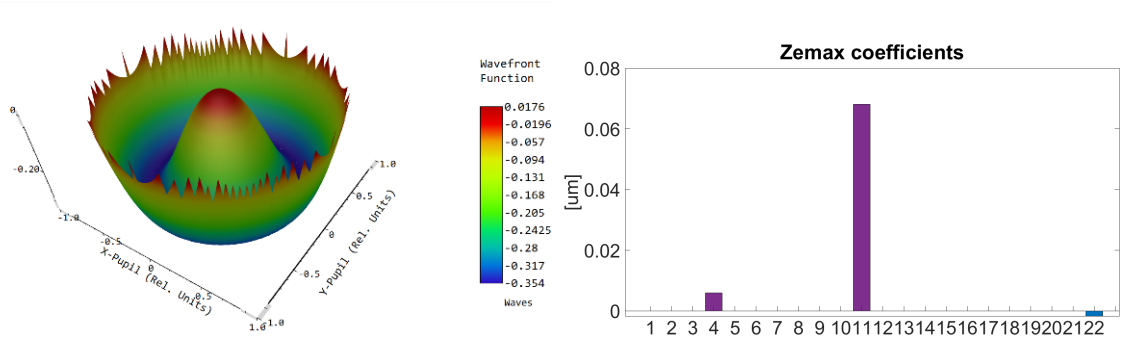


Figure 6.37: The wavefront on the output of the modeled optical system, generated by Zemax.

The wavefront on the output of the aligned optical system measured in the laboratory can be seen in figure 6.38. The value of the coefficient is slightly different compared to the Zemax model, however, this can be caused by a slightly different definition of the aperture. The real system is not as perfectly aligned as the computer model, hence another source of error is introduced. On top of that, there is a noise of the reconstruction algorithm present. Lenses used in the system also have some aberration, which is affecting the output wavefront.

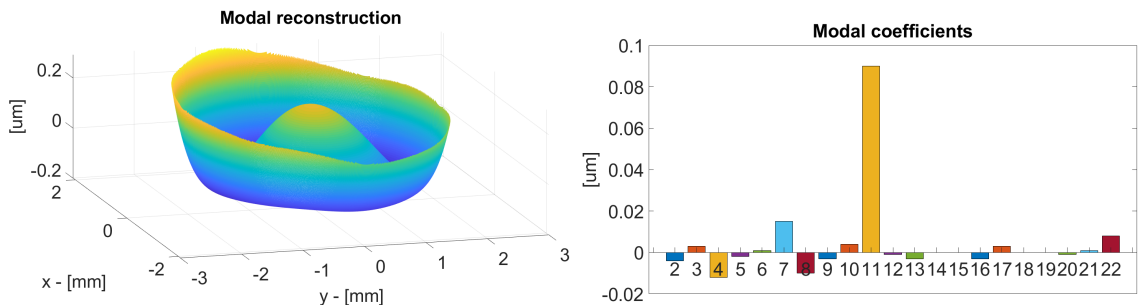


Figure 6.38: The wavefront on the output of the real optical system measured in the laboratory.

Important fact is that the shape of the real wavefront on the output of the system is almost similar to the simulated one. The most dominant coefficient is C_{11} - primary spherical aberration in both cases. The algorithm for alignment of the complex optical systems was in early stage of development, therefore, there are no further results presented in this thesis. However, the wavefront sensor is giving promising results and it should play a major role in the further development.

6 Application of the Algorithm for Wavefront Reconstruction of the Structured Beam

Non-diffractive beams are the solutions to the Helmholtz equation, that have different properties compared to well-known Gaussian beams. As the name suggests, their transverse profile does not change as they propagate, hence they have a very low divergence. Another interesting property is the self-regeneration effect behind the obstacle. This is due to the fact, that non-diffractive beams are interference fields [36].

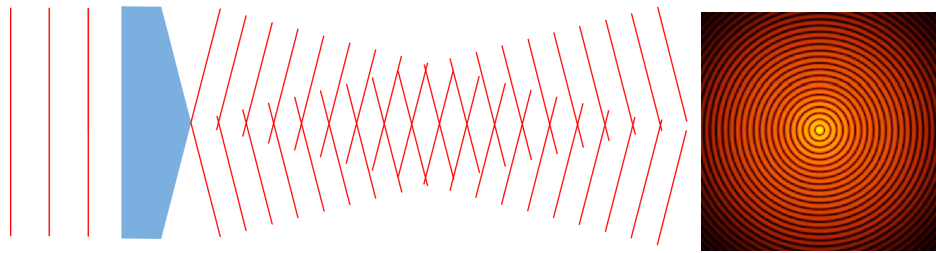


Figure 7.39: Generation of a Bessel beam using an axicon (left) and its transversal intensity profile [37] (right). We can see, that there is a limited distance, where the plane waves intersect hence interfere and form the Bessel beam.

The problem with Bessel beams is their limited propagation distance, due to the principle of their generation using axicon. The Structured beam is a novel type of non-diffractive, that has been patented in the last years in collaboration between TOPTEC and CERN by Miroslav Šulc and Jean-Christophe Gayde.

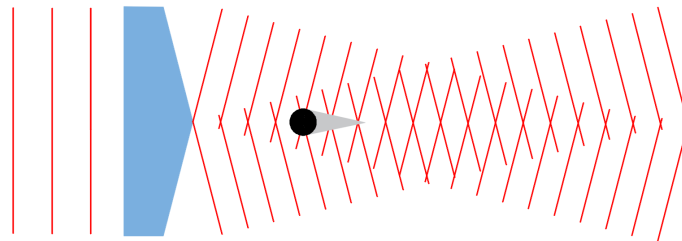


Figure 7.40: Illustration of a self-regenerating ability of Bessel beams. There is a small grey "shadow" behind the circular obstacle, where the beam is not generated, however, the beam regenerates when it overcomes it, due to the fact that the plane waves are tilted with respect to the direction of propagation.

The Structured beam is again an interference field with the transversal intensity profile almost similar to a Bessel beam. However, it can be generated using the optical aberrations of thick and thin convex lenses, namely spherical aberration and defocus. This allows it to overcome the propagation distance limitation while maintaining its transversal profile and low divergence. These properties give it

the potential to be used in various applications. More about the principle of the generation and other information about the Structured beam can be found in [37, 38, 39, 40].

6.1 Wavefront reconstruction of the Structured beam

Structured beams are still the subject of intensive research. Numerical simulations that predict the wavefront shape (figure 7.41) have been presented in [37], backed up with the reconstruction using a SHWS WFS-150-5C by Thorlabs. However, the results of the reconstruction were suboptimal. Therefore, we decided to redo the experiment.

First, we used the SHWS WFS30-7AR and software by Thorlabs. We were not able to reconstruct the wavefront properly, as we can see in figure 7.42. We believe this is due to the complex spotimage of the Structured beam (figure 7.43). The software by Thorlabs uses an unknown algorithm for the detection of the spot centroids and reconstruction.

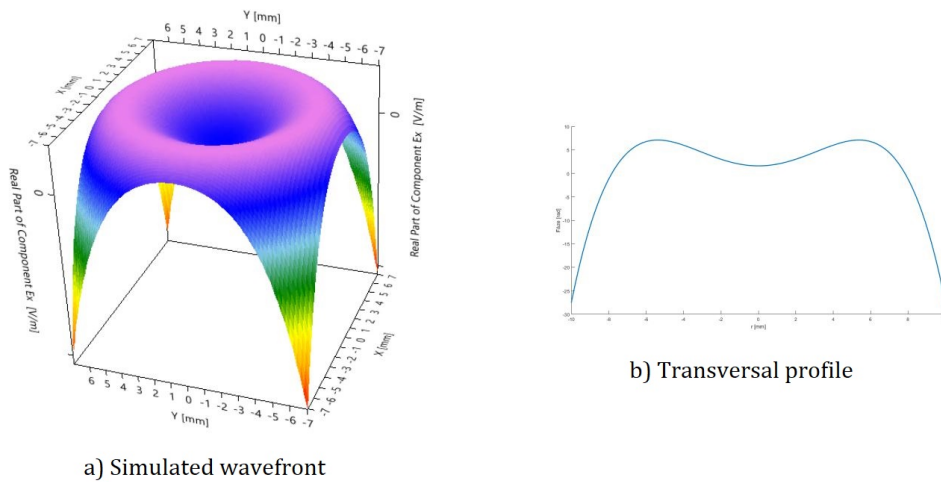


Figure 7.41: Simulation of a wavefront of a Structured beam using VirtualLab Fusion [37].

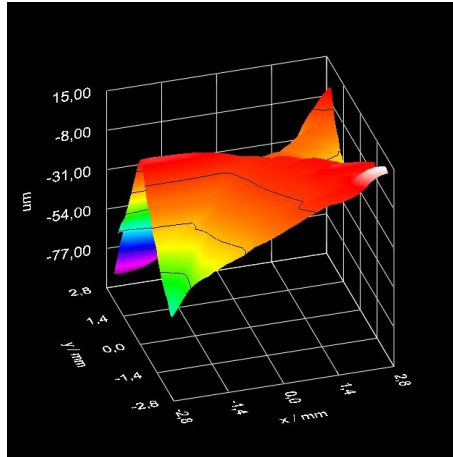


Figure 7.42: The reconstructed wavefront of the Structured beam using the Thorlabs software. The reconstruction is very noisy and the wavefront does not match the simulation.

Therefore, we used the presented software to reconstruct the wavefront using the correlation centroiding algorithm (chapter 3.1.4). It was able to suppress the noise and locate the proper centroids of the actual spots.

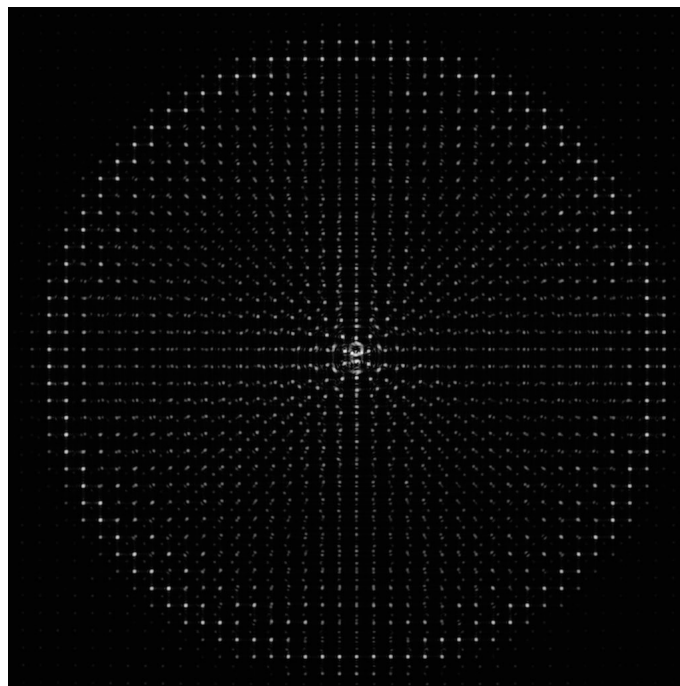


Figure 7.43: Spotimage generated by a Structured beam. A lot of noise and pseudo spots can be seen.

If we compare the reconstructed wavefront in figure 7.44 and the simulated wavefront in figure 7.41, we can say, that the shape and transversal profile are

similar. As stated in the previous chapter, the generator of a Structured beam utilizes defocus and spherical aberration. If we look at results of the reconstruction, the most dominant Zernike coefficients are C_4 , C_{11} and C_{22} which are defocus, primary spherical aberration and secondary spherical aberration respectively. This fact also backs up the results.

Reconstructing the wavefront of the Structured beam opens new possibilities in the research of this topic.

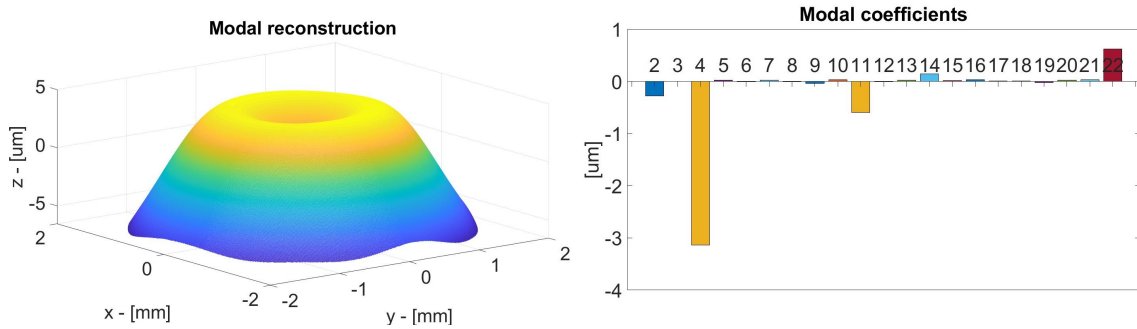


Figure 7.44: If we compare the results with figure 7.41, the shape of the reconstructed wavefront is matching the simulations. The most dominant Zernike coefficients are C_4 , C_{11} and C_{22} which are defocus, primary spherical aberration and secondary spherical aberration respectively.

7 Conclusions

The theoretical part is briefly describing the necessary background and principle of SHWS wavefront reconstruction to make it easier for the reader to understand the experimental part. The principal limitations of the sensor are also presented.

Afterward, the developed algorithms for the wavefront reconstruction are described in great detail. One of the implemented features is the novel calibration routine that also includes the process for the compensation of the manufacturing errors of the sensor, which leads to the extremely high precision of the reconstructions. The calibration process makes it possible to calibrate any SHWS with any given parameters, making the software versatile. This is a very important fact for TOPTEC, because there will be a possibility to manufacture various sensors indoors, based on the needs of the different experimental applications.

Four centroiding algorithms, two fitting algorithms and other features are included in the software. Therefore, it is possible to choose the exact parameters of the reconstruction depending on the nature of the experiment.

All of the algorithms were analyzed in terms of time efficiency and reconstruction accuracy. Simulation routines were developed for this task. The results of the simulations show that the gamma algorithm seems to be the best choice for the detection of the spot centroids in the majority of cases. Analysis of the fitting algorithms shows the superiority of the modal routine to the zonal one.

Experimental measurements of five various wavefronts were done and compared with the results from certified commercial software by Thorlabs. The difference between the reconstructed wavefronts is usually around 15 nm RMSe depending on the aperture size. This means that the presented software is a solid alternative to the commercial one.

The software was also used as a part of the experimental algorithm for the alignment of the complex optical systems. The MATLAB code was compiled into .NET library to make it possible to use it in C#. This enabled new functionality such as real-time wavefront reconstruction. There was also a need for the variability of the axis orientation, hence it was implemented. The commercial software does not offer this feature. The outcomes of the reconstructions were compared to the simulations carried out with Zemax software and the similarity in results proves the high accuracy of the sensor.

Lastly, the software was able to reconstruct the wavefront of the Structured beam using the correlation centroiding algorithm. The shape of the wavefront correlates with the simulations and theoretical assumptions about the Structured beam. This has never been done before because the commercial software failed in this task. Reconstructing the wavefront of the Structured beam opens new possibilities in the research of this topic.

The software offers tremendous potential in various experimental applications in TOPTEC, thanks to the variability of the wavefront reconstruction parameters while maintaining the high accuracy of the reconstruction. The developed calibration routine opens a possibility for manufacturing sensors indoors. The software has been and will be used for the alignment of the complex optical systems and reconstruction

of the wavefront of the Structured beam. The literature shows [23, 24] that there is a possibility to increase the dynamic range of the sensor using the specialized algorithms. Therefore, future implementation of this feature can offer lead to even better performance of the software compared to the commercial alternatives.

Bibliography

- [1] Platt, Brennan C. and Robert Bruce Shack, History and principles of Shack-Hartmann wavefront sensing, *Journal of refractive surgery*, vol. 17, no. 5, pp. 573-577. 2001.
- [2] Rukosuev, A.L., Kudryashov, A.V., Lylova, A.N. et al. Adaptive optics system for real-time wavefront correction. *Atmos Ocean Opt*, 28, 2015. <https://doi.org/10.1134/S1024856015040119>
- [3] J. Novak, A. Misk, Application of Shack-Hartmann wavefront sensor for testing optical systems, *Proceedings of SPIE - The International Society for Optical Engineering*, 6609, 2007.
- [4] DAI, Guang-ming, *Wavefront Optics for Vision Correction*, Society of Photo-Optical Instrumentation Engineers, 2008. DOI: 10.1117/3.769212. ISBN: 9780819469663.
- [5] B. E. A. Saleh, *Fundamentals of Photonics*. Matfyzpress, Prague, 1994.
- [6] M. Born, E. Wolf. *Principles of optics*, 6th ed. Pergamon Press, New York, 1980.
- [7] Faculty of Mathematics and Physics, Charles University, *Introduction to ray optics*, [online]. Available: https://physics.mff.cuni.cz/kfpp/skripta/kurz_fyziky_pro_DS/www/fyzika.html
- [8] V.N. Mahajan, *Optical imaging and aberrations: Part II: Wave diffraction optics: Second edition*, 2001. 10.1117/3.898443.
- [9] Geary, Joseph M, *Introduction to wavefront sensors*, SPIE Optical Engineering Press Bellingham, Washington, USA, 1995.
- [10] T. B. Andersen, Efficient and robust recurrence relations for the Zernike circle polynomials and their derivatives in Cartesian coordinates, *Opt. Express*, 26, 18878-18896, 2018.
- [11] L. Vasudevan, F. Andre, Zernike polynomials: A guide, *Journal of Modern Optics*, 58. 1678-1678, 2011. DOI: 10.1080/09500340.2011.633763.

- [12] Wikipedia, *Zernike polynomials*, 2020. [Online]. Available: https://en.wikipedia.org/wiki/Zernike_polynomials
- [13] R. J. Noll, Zernike polynomials and atmospheric turbulence, *J. Opt. Soc. Am.* 66 (3): 207, 1976. doi:10.1364/JOSA.66.000207
- [14] J. Hartmann, Bemerkungen uber den Bau und die Justirung von Spektrografen, *Zt. Instrumentenk.*, vol. 20, pp 47-58. 1900.
- [15] Wyant, James and Creath, Katherine, Basic Wavefront Aberration Theory for Optical Metrology, *Appl Optics Optical Eng.*, vol. 11. 1992.
- [16] L. A. Poyneer, Advanced techniques for Fourier transform wavefront reconstruction, *Adaptive Optical System Technologies II, Proc. SPIE*, 4839. 2002.
- [17] Hong Guo, Nina Korablinova, Qiushi Ren, and Josef Bille, Wavefront reconstruction with artificial neural networks, *Opt. Express* 14, 6456-6462. 2006.
- [18] Panagopoulou, S. I., and Neal, D. R, *Zernike vs. zonal matrix iterative wavefront reconstructor*, 2014.
- [19] W. H. Southwell, Wave-front estimation from wave-front slope measurements, *Journal of the Optical Society of America*, vol. 70, no. 8, p. 998. 1980.
- [20] W Zou and J. P. Rolland, Quantifications of error propagation in slope-based wavefront estimations, *Journal of the Optical Society of America A*, vol. 23, no. 10, p. 2629, Oct. 2006.
- [21] I. B. Apaolaza, *Characterization of optical aberrations: Practical Implementation of a SHACK-HARTMANN Sensor with MATLAB*. Master's Thesis. Available: http://academica-e.unavarra.es/bitstream/handle/2454/35010/TFG_I%C3%B1igo_Belio_Apaolaza.pdf?sequence=1&isAllowed=y
- [22] C. Curatu etl al., Fundamental and specific steps in Shack-Hartmann wavefront sensor design, *Proc. SPIE 6288, Current Developments in Lens Design and Optical Engineering VII*, 628801. 2006. DOI: 10.1117/12.680892
- [23] D.G. Smith, *High Dynamic Range Calibration for an Infrared Shack-Hartmann Wavefront Sensor*. Dissertation. University of Arizona. 2008. Available: <https://repository.arizona.edu/handle/10150/194779>
- [24] J. Pfund et. al., Dynamic range expansion of a Shack-Hartmann sensor by use of a modified unwrapping algorithm, *Optics Letters*, vol. 23, no. 13, p. 995. 1998.

- [25] John C. Russ, *The image processing handbook*. CRC Press. 2007. ISBN 978-0-8493-7254-4.
- [26] Poynee, L. A., *Correlation Wave-Front Sensing Algorithms for Shack-Hartmann-Based Adaptive Optics using a Point Source*. 2003.
- [27] X. Li, X. Li, and C. wang, Improvement of correlation-based centroiding methods for point source Shack–Hartmann wavefront sensor, *Optics Communications*, vol. 411, pp. 187–194, 2018.
- [28] A. Chernyshov et. al., Calibration of a Shack–Hartmann sensor for absolute measurements of wavefronts, *Appl. Opt.* 44, 6419-6425. 2005.
- [29] J. Yang et. al., Absolute calibration of Hartmann-Shack wavefront sensor by spherical wavefronts, *Optics Communications*. 283, 910-916. 2010. DOI: 10.1016/j.optcom.2009.11.022.
- [30] A. Nikitin et. al., Absolute calibration of a Shack-Hartmann wavefront sensor for measurements of wavefronts, *Proc. SPIE* 10925, Photonic Instrumentation Engineering VI, 109250K. 2019. DOI: 10.1117/12.2510047.
- [31] Thorlabs, *Optical Wavefront Sensors Operation Manual.*, 2020. https://www.thorlabs.com/drawings/f165a0c0dc5723a9-B9DE88A3-940F-4B09-0E0201F343A36E5C/WFS30-14AR_M-Manual.pdf
- [32] Robert Gray, ZernikeCalc (<https://www.mathworks.com/matlabcentral/fileexchange/33330-zernikecalc>), MATLAB Central File Exchange. Retrieved October 3, 2020.
- [33] Thomas Dideriksen, Custom 2D Gauss (<https://www.mathworks.com/matlabcentral/fileexchange/9556-custom-2d-gauss>), MATLAB Central File Exchange. Retrieved October 1, 2020.
- [34] R. Navarro, J. Arines, Complete Modal Representation with Discrete Zernike Polynomials - Critical Sampling in Non Redundant Grids, *Numerical Simulations of Physical and Engineering Processes*. IntechOpen. 2011. DOI: 10.5772/24631. <https://cdn.intechweb.org/pdfs/20891.pdf>
- [35] N. Patel, C. S. Narayanamurthy, Measurement of optical misalignment using wavefront sensing, *Optical Engineering*, 54(10), 104106. doi:10.1117/1.oe.54.10.104106
- [36] D. L. Andrews, *Structured Light and Its Applications: An Introduction to Phase-Structured Beams and Nanoscale Optical Forces*, Academic Press, 2008. ISBN 9780123740274.

- [37] K. Polák, *Optimizing of properties of structured optical beams*, Master's Thesis. Technical University of Liberec. 2018.
- [38] J. Junek, *Spatial distribution of structured optical beams of near wavelengths*, Master's Thesis. Technical University of Liberec. 2018.
- [39] D. Jínová, *Structured beams for optical elements alignment*, Master's Thesis. Technical University of Liberec. 2018.
- [40] J. Křížek, *Study of non-diffracting beams*, Master's Thesis. Czech Technical University in Prague. 2016